



# Experimental validation of theoretical methods to estimate the energy radiated by elastic waves during an impact

Maxime Farin, Anne Mangeney, Julien De Rosny, Renaud Toussaint, Jacques Sainte-Marie, Nikolai M. Shapiro

## ► To cite this version:

Maxime Farin, Anne Mangeney, Julien De Rosny, Renaud Toussaint, Jacques Sainte-Marie, et al.. Experimental validation of theoretical methods to estimate the energy radiated by elastic waves during an impact. To be published in Journal of Sound and Vibration. 2015. <hal-01213752>

**HAL Id: hal-01213752**

**<https://hal.archives-ouvertes.fr/hal-01213752>**

Submitted on 8 Oct 2015

**HAL** is a multi-disciplinary open access archive for the deposit and dissemination of scientific research documents, whether they are published or not. The documents may come from teaching and research institutions in France or abroad, or from public or private research centers.

L'archive ouverte pluridisciplinaire **HAL**, est destinée au dépôt et à la diffusion de documents scientifiques de niveau recherche, publiés ou non, émanant des établissements d'enseignement et de recherche français ou étrangers, des laboratoires publics ou privés.



# Experimental validation of theoretical methods to estimate the energy radiated by elastic waves during an impact

Maxime Farin<sup>a,\*</sup>, Anne Mangeney<sup>a,1</sup>, Julien de Rosny<sup>c</sup>, Renaud Toussaint<sup>d</sup>,  
Jacques Sainte-Marie<sup>b</sup>, Nikolai M. Shapiro<sup>a</sup>

<sup>a</sup>*Institut de Physique du Globe de Paris, Sorbonne Paris Cité, CNRS (UMR 7154)*

<sup>b</sup>*ANGE team, CEREMA, Inria, Lab. J.-L. Lions, CNRS*

<sup>c</sup>*ESPCI, Institut Langevin, CNRS, 1 rue Jussieu, 75005 Paris.*

<sup>d</sup>*Institut de Physique du Globe de Strasbourg, Université de Strasbourg / EOSt, CNRS,  
5 rue Descartes, F-67084 Strasbourg Cedex, France.*

---

## Abstract

Estimating the energy lost in elastic waves during an impact is an important problem in seismology and in industry. We propose three complementary methods to estimate the elastic energy radiated by bead impacts on thin plates and thick blocks from the generated vibration. The first two methods are based on the direct wave front and are shown to be equivalent. The third method makes use of the diffuse regime. These methods are tested for laboratory experiments of impacts and are shown to give the same results, with error bars from 40% to 300% for impacts on a smooth plate and on a rough block, respectively. We show that these methods are relevant to establish the energy budget of an impact. On plates of glass and PMMA, the radiated elastic energy increases from 2% to almost 100% of the total energy lost as the bead diameter approaches the plate thickness. The rest of the

---

\*Corresponding author

*Email address:* farin@ipgp.fr, +33 1 83 95 77 82 (Maxime Farin)

lost energy is dissipated by viscoelasticity. For beads larger than the plate thickness, plastic deformation occurs and reduces the amount of energy radiated in the form of elastic waves. On a concrete block, the energy dissipation during the impact is principally inelastic because only 0.2% to 2% of the energy lost by the bead is transported by elastic waves. The radiated elastic energy estimated with the presented methods is quantitatively validated by Hertz's model of elastic impact.

*Keywords:* elastic waves, acoustic generation, impact source, energy budget

*PACS:* [2010] 46.40.-f

---

Table 1: Nomenclature

$B$	Bending stiffness (J)
$c_P, c_S, c_R$	Longitudinal, shear and Rayleigh wave speeds ( $\text{m s}^{-1}$ )
$e$	Coefficient of restitution (-)
$e_{tot}, e_c, e_p$	Bulk densities of total, kinetic and potential energies ( $\text{J m}^{-3}$ )
$\tilde{e}_{tot}, \tilde{e}_c, \tilde{e}_p$	Time Fourier transform of $e_{tot}, e_c, e_p$ , respectively ( $\text{J m}^{-2}$ )
$E$	Young's modulus (Pa)
$E_c, \Delta E_c$	Energy of the impact and energy lost during the impact (J)
$E_{tot}(t)$	Total elastic energy radiated within the structure at time $t$ (J)
$f$	Frequency ( $\text{s}^{-1}$ )
$\tilde{G}_{zz}^P, \tilde{G}_{zz}^S, \tilde{G}_{zz}^R$	Vertical Green's functions associated with compressional, shear and Rayleigh waves ( $\text{kg}^{-1} \text{s}^2$ )
$h$	Plate thickness (m)
$k$	Wave number ( $\text{m}^{-1}$ )
$L, S, V$	Length (m), surface area ( $\text{m}^2$ ) and volume ( $\text{m}^3$ )
$m$	Bead mass (kg)
$r, \theta, z$	Coordinates in the cylindrical reference frame (m)
$S_{ij}$	Strain tensor (-)
$t$	Time (s)
$T_{ij}$	Stress tensor (Pa)
$\mathbf{u}_i$	Normalized vector of direction $i$
$u_i, v_i, a_i$	Surface displacement, speed and acceleration in the direction $\vec{u}_i$ (m; $\text{m s}^{-1}$ ; $\text{m s}^{-2}$ )

$\tilde{U}_i, \tilde{V}_i, \tilde{A}_i$	Time Fourier transform of $u_i, v_i$ and $a_i$ , respectively (m s; m; m s <sup>-1</sup> )
$v_g, v_\phi$	Group and phase velocities (m s <sup>-1</sup> )
$V_z$	Speed of a bead before impact (m s <sup>-1</sup> )
$W_{el}, W_{el}^{th}$	Radiated energy and theoretical radiated energy (J)
$x, y, z$	Coordinates in the Cartesian reference frame (m)
$\beta, \xi$	Parameters involved in energy calculations
$\gamma$	Attenuation coefficient of energy with distance (m <sup>-1</sup> )
$\lambda, \mu$	Lamé coefficients of compression and shear (Pa)
$\nu$	Poisson's coefficient (-)
$\pi_P, \pi_S, \pi_R$	Energy partitions among $P, SV$ and Rayleigh waves (-)
$\pi_P^{surf}, \pi_S^{surf}, \pi_R^{surf}$	Surface energy partitions among compressional, shear and Rayleigh waves (-)
$\tilde{\Pi}$	Energy density flux (J m <sup>-1</sup> s)
$\rho$	Density (kg m <sup>3</sup> )
$\tau$	Characteristic time of energy attenuation (s)
$\chi, \eta$	Viscoelastic coefficients of compression and shear (Pa s)
$\omega$	Angular frequency (s <sup>-1</sup> )

## 1. Introduction

The quantification of the energy emitted by a source in the form of elastic waves is a common problem in various fields such as vibroacoustics or shielding. In seismology, the problem was confronted long ago [1] and many approaches have since been developed to estimate the energy of natural sources such as earthquakes [see 2, 3, 4, 5], tremors [6], landslides and rockfalls [e.g. 7, 8, 9, 10, 11]. In the literature, the power spectral density (PSD) of the emitted signal is often measured to quantify the relative energy of different acoustic sources located at the same distance from the sensor and to compare their frequency content. For example, the temporal evolution of the PSD can provide information on river discharge and on the grain size of the bed load [e.g. 12]. The PSD can also be used to characterize crack formation in brittle [13, 14] or granular materials [see 15, for review] and other crackling or crumpling processes [e.g. 16, 17]. Finally, acoustic measurements can be useful in industry for particle sizing in powder transport and in particle streams [e.g. 18, 19]. However, the PSD does not provide an absolute estimate of the elastic energy radiated by the source because it depends on the distance of measurement.

There are three main approaches to determine the absolute radiated elastic energy from acoustic emissions. The first method consists in computing the energy flux crossing a surface surrounding the source. The integration of the energy flux over this surface gives the radiated power. This technique is applied in seismology to estimate the energy radiated in elastic waves during earthquakes [e.g. 5, 20] and rockfalls [e.g. 8, 9, 10].

The second technique to deduce the radiated elastic energy is based on

26 the estimation of the time dependence of the source force. Miller and Pursey  
27 [21] and Goyder and White [22] thus estimated the power radiated in an  
28 elastic half-space and in an infinite plate, respectively, by a monochromatic  
29 harmonic force. In most cases, the force profile is generally unknown but it  
30 can be retrieved from the deconvolution of the displacement field with the  
31 Green's function tensor [3].

32 These two first methods can however be performed only when the emitted  
33 wave front is not mixed with its reflections off the boundaries of the elastic  
34 solid. If multiple side reflections occur, the transported energy becomes ho-  
35 mogeneously distributed within the elastic solid and decreases exponentially  
36 with time due to viscoelastic dissipation. This situation is commonly referred  
37 to as a diffuse field in the literature [see 23, 24, 25]. A third energy estimation  
38 method, called the diffuse method hereafter, thus consists in extrapolating  
39 the radiated energy at the instant of the source from the exponential decrease  
40 of the signal coda [see e.g. 25, 26, and references therein].

41 The energy flux, deconvolution and diffuse field methods to estimate the  
42 energy lost in elastic waves are used separately by different communities  
43 and are based on different assumptions. The first two methods require a  
44 sufficiently large elastic solid so that the direct wave front can be clearly  
45 distinguished from its reflections off the lateral sides of the elastic solid. On  
46 the contrary, with the diffuse method, the elastic solid must be small enough  
47 so that multiple side reflections occur. To our knowledge, no study has ever  
48 compared these three methods in cases where all three can be applied.

49 The complex seismic signals generated by rockfalls, bed load transport in  
50 rivers and granular flows are partially composed of waves generated by the



51 collisions of individual impactors (gravels, boulders,...). Therefore, if we hope  
52 to understand these signals, we must first understand the energy budget of  
53 individual impacts. The energy that is not radiated in elastic waves during  
54 an impact is lost by plastic deformation i.e., not reversible, of the impactor  
55 or of the surface [27], by local viscoelastic dissipation around the contact [28]  
56 and by conversion into other degrees of freedom of the impactor's motion,  
57 such as rotation and other displacement modes. Because of the significant  
58 differences between the conditions of each impact on the field, it is however  
59 not clear how the energy budget of the impactor depends on its size and  
60 speed.

61 In this paper, we propose to use the three methods introduced above  
62 to estimate the elastic energy radiated during an individual impact. Steel  
63 beads of various diameters are dropped from different heights on two glass  
64 and PMMA plates and on a concrete block and the vibration emitted by the  
65 impacts is measured with piezoelectric accelerometers. Our main objective  
66 is to quantify (i) the differences between the energy estimates and (ii) the  
67 errors made using each of the methods. Thin plates are often used in labo-  
68 ratory experiments because they are easier to manipulate than thick blocks.  
69 In contrast, the problem of waves generation in thick blocks is that encoun-  
70 tered on the field. We will show that the methods to estimate the radiated  
71 elastic energy in these two geometries are different because different waves  
72 are generated. An advantage of the laboratory experiments is that the total  
73 energy lost by a rebounding bead can be easily measured from the ratio of  
74 the bead velocity after rebound over the approach velocity, i.e. the coefficient  
75 of restitution  $e$  [e.g. 28]. Therefore, we can establish the energy budget of

76 the impacts and observe how the percentages of energy radiated in elastic  
77 waves and dissipated by inelastic processes vary for bead impacts of different  
78 diameters and impact speeds on the thin plates and thick block investigated.

79 Section 2 of the paper presents the three methods to derive the energy  
80 lost in elastic waves during an impact on thin plates and thick blocks from  
81 the normal surface vibration. In section 3, the three methods are compared  
82 for laboratory experiments of beads impacts. We also quantify the propor-  
83 tion of the total energy radiated in elastic waves and dissipated in inelastic  
84 processes. In section 4, we discuss the conditions of applicability of the pre-  
85 sented methods. Finally, we evaluate the ability of the analytical model of  
86 elastic impact of Hertz [29] [see 30] to predict the radiated elastic energy and  
87 the ratio of this energy over the initial energy of the impactor when inelastic  
88 dissipation occurs.

## 89 **2. Estimation of the radiated elastic energy**

### 90 *2.1. Thin plates*

91 A force  $\mathbf{F}(t) = -F_z(t)\mathbf{u}_z$  is applied normally at a given position  $(x, y, 0)$   
92 on the surface ( $z = 0$ ) of a homogeneous and isotropic thin plate (Figure 1).  
93 The expression “thin plate” means that the impact duration is longer than  
94 the two-way travel time of the compressional wave in the plate thickness. The  
95 emitted elastic waves propagate radially from the impact location (direction  
96  $\mathbf{u}_r$ , Figure 1). We consider that the principal mode excited in plates is  
97 the fundamental mode  $A_0$  of Lamb, for which the direction of vibration is  
98 mainly normal to the plate surface (i.e. direction  $\mathbf{u}_z$ , Figure 1) [e.g. 35]. This  
99 assumption is verified experimentally in Appendix A. For all the methods

100 tested below, it is therefore assumed that the vibration is only along direction  
 101  $\mathbf{u}_z$  (Figure 1).

102 The mode  $A_0$  of Lamb is highly dispersive at low frequencies, when the  
 103 wavelength is much greater than the plate thickness  $h$ , i.e. within the limit  
 104  $kh \ll 1$  where  $k$  is the wave number. Indeed, in this regime the mode  
 105  $A_0$  behaves as a flexural wave for which the relation between the angular  
 106 frequency  $\omega$  and the wave number  $k$ , i.e. the dispersion relation is [35]:

$$107 \quad \omega = k^2 \sqrt{\frac{B}{\rho h}}, \quad (1)$$

108 where  $\rho$  is the plate density. The bending stiffness  $B$  is defined by  $B =$   
 109  $h^3 E / (12(1 - \nu^2))$ , where  $E$  and  $\nu$  are the Young's modulus and Poisson's ratio  
 110 of the plate material, respectively. The propagation speed of the energy, i.e.  
 111 the group velocity  $v_g = \partial\omega / \partial k$ , therefore also depends on the wave number  
 112  $k$  (i.e. on the angular frequency  $\omega$ ):

$$113 \quad v_g(\omega) = 2k \sqrt{\frac{B}{\rho h}}. \quad (2)$$

#### 114 2.1.1. Energy flux method

115 The first method to estimate the radiated elastic energy is based on en-  
 116 ergy flux conservation on the first wave arrival. The energy density flux  
 117  $\tilde{\Pi}(\omega)$  at frequency  $\omega$  is by definition the bulk density of the total energy  
 118  $\tilde{e}_{tot}(\omega) = \tilde{e}_c(\omega) + \tilde{e}_p(\omega)$ , integrated over plate thickness  $h$ , multiplied by the  
 119 energy speed. But for elastic waves propagating in a homogeneous guide (for  
 120 example a plate) such as the  $A_0$  mode, the energy speed is equal to the group  
 121 velocity  $v_g(\omega)$  [35], so that:

$$122 \quad \tilde{\Pi}(\omega) \hat{=} v_g(\omega) \int_{-h/2}^{h/2} \tilde{e}_{tot}(\omega) dz. \quad (3)$$

123 Moreover, for guided waves the bulk densities of kinetic and potential energies  
 124  $\tilde{e}_c(\omega)$  and  $\tilde{e}_p(\omega)$  are equal [e.g. 35]:

$$125 \quad \tilde{e}_c(\omega) = \tilde{e}_p(\omega) = \frac{1}{2}\rho|\tilde{V}_z(r,\omega)|^2, \quad (4)$$

126 where  $\tilde{V}_z(r,\omega)$  is the time Fourier transform of the surface vibration speed  
 127  $v_z(r,t)$ .

128 By definition, the elastic energy  $W_{el}$  radiated within the plate is given by  
 129 [e.g. 35]:

$$130 \quad W_{el} \hat{=} \int_{-\infty}^{+\infty} F_z(\mathbf{r}_0, t)v_z(\mathbf{r}_0, t)dt, \quad (5)$$

131 where  $\mathbf{r}_0$  is the position of force application. According to Parseval's theorem,  
 132 this expression is equivalent to the integral over the frequencies  $\omega$  of the  
 133 radiated power, which is the flux  $\tilde{\Pi}(\omega)$  integrated over a line surrounding the  
 134 impact:

$$135 \quad W_{el} = \frac{1}{2\pi} \int_{-\infty}^{+\infty} \left[ \oint \tilde{\Pi}(\omega) r d\theta \right] d\omega \quad (6)$$

$$136 \quad W_{el} = \frac{1}{\pi} \int_0^{+\infty} \left[ v_g(\omega) \iint_S \rho |\tilde{V}_z(r,\omega)|^2 r d\theta dz \right] d\omega. \quad (7)$$

137 As waves propagate radially from the source, one can integrate the surface  
 138 element  $r d\theta dz$  over a cylinder of height equal to the plate thickness  $h$  and  
 139 of radius equal to the distance  $r$  between the impact and the position of  
 140 measurement (Figure 1). In equation (7), the distance  $r$  compensates the  
 141 geometrical attenuation in  $1/r^{1/2}$  of the vibration amplitude  $\tilde{V}_z(r,\omega)$  of the  
 142 guided wave. In addition, other dissipation is due to the intrinsic viscosity of  
 143 the plate. This dissipation can be modeled by  $\exp(-\gamma(\omega)r)$ , where  $\gamma$  is the  
 144 coefficient representing the frequency-dependent attenuation of energy with

145 distance  $r$  in the plate (see Appendix B):

$$146 \quad W_{el} = \int_0^{+\infty} 2rh\rho v_g(\omega) |\tilde{V}_z(r, \omega)|^2 \exp(\gamma(\omega)r) d\omega. \quad (8)$$

147 Note that if we consider a constant group velocity  $v_g$ , we obtain an expression  
 148 for  $W_{el}$  similar to that used by Hibert et al. [10] to estimate the energy of  
 149 surface waves generated by rockfalls in a homogeneous surface layer of depth  
 150  $h$  in Dolomieu crater, Réunion Island.

### 151 2.1.2. Deconvolution method

152 As opposed to the energy flux method, here we compute the radiated elas-  
 153 tic energy  $W_{el}$  using equation (5) from the estimation of the time dependence  
 154 of the force of impact. Indeed, the energy  $W_{el}$  transferred into the plate at  
 155 the point of application of a normal force  $F_z(\mathbf{r}_0, t)$  is the time integral of the  
 156 radiated power, which is given by Goyder and White [22]:

$$157 \quad \mathbf{F}(\mathbf{r}_0, t) \cdot \mathbf{v}(\mathbf{r}_0, t) = \frac{F_z(\mathbf{r}_0, t)^2}{8\sqrt{B\rho h}}. \quad (9)$$

158 Then, according to Parseval's theorem,

$$159 \quad W_{el} = \frac{1}{\pi} \int_0^{+\infty} \frac{|\tilde{F}_z(\omega)|^2}{8\sqrt{B\rho h}} d\omega. \quad (10)$$

160 We can deduce the normal force  $\tilde{F}_z(\omega)$  in time Fourier domain from the  
 161 expression of the first arrival of the vertical vibration speed  $\tilde{V}_z(r, \omega)$  as a  
 162 function of the plate Green's function  $\tilde{G}_{zz}(r, \omega)$  [3]:

$$163 \quad \tilde{V}_z(r, \omega) = i\omega \tilde{G}_{zz}(r, \omega) \tilde{F}_z(\omega), \quad (11)$$

164 where the modulus of the plate Green's function can be approximated by,  
 165 for  $kr \gg 1$  [e.g. 36]:

$$166 \quad |\tilde{G}_{zz}(r, \omega)| = \frac{1}{8Bk^2} \sqrt{\frac{2}{\pi kr}} \quad (12)$$

167 Finally, the radiated elastic energy  $W_{el}$  is given by:

$$168 \quad W_{el} = \frac{1}{8\pi\sqrt{B\rho h}} \int_0^{+\infty} \omega^{-2} \frac{|\tilde{V}_z(r, \omega)|^2}{|\tilde{G}_{zz}(r, \omega)|^2} \exp(\gamma(\omega)r) d\omega. \quad (13)$$

169 where  $\exp(-\gamma(\omega)r)$  models the viscoelastic dissipation.

170 Interestingly, if we replace the Green's function  $|\tilde{G}_{zz}(r, \omega)|$  by its expres-  
 171 sion [equation (12)], we retrieve the same expression of  $W_{el}$  as for the energy  
 172 flux method under the condition that  $\omega = k^2\sqrt{B/\rho h}$ , which is valid for  
 173  $kh \ll 1$ . Therefore, the two methods are equivalent at low frequencies  
 174  $\omega \ll \sqrt{B/\rho h}/h^2$ .

175 Note that the operation of dividing the amplitude of the vibration  $|\tilde{V}_z(r, \omega)|$   
 176 by the Green's function  $|\tilde{G}_{zz}(r, \omega)|$  is not trivial because the inverse Green's  
 177 function diverges when  $k$  (or  $\omega$ ) tends towards 0 [see e.g. 31, 37]. Therefore,  
 178 we cannot deconvolve the signal and estimate the energy  $W_{el}$  below a cutoff  
 179 frequency. In practice, we cut all frequencies below 3 kHz in the amplitude  
 180 spectrum  $|\tilde{V}_z(r, \omega)|$  before dividing it by the Green's function. Using a syn-  
 181 thetic signal obtained by the convolution of the Hertz force for the elastic  
 182 impact of bead diameters smaller than 20 mm with the Green's function in  
 183 equation (12), we estimate that the energy  $W_{el}$  of the signal after the cut-  
 184 off at 3 kHz is less than 5% smaller than the exact radiated elastic energy  
 185 (Figure 2).

### 186 2.1.3. Diffuse method

187 This technique is derived from classical methods used in room acoustics  
 188 [see e.g. 25, and references therein]. When the emitted wave is reflected off  
 189 the boundaries many times, the elastic field becomes diffuse, i.e. homoge-  
 190 neously distributed over the plate and equipartitioned. When the field is

191 equipartitioned, the potential and kinetic energy are equal. At a given time  
 192  $t$ , the average over several periods (noted  $\bar{x}$ ) of the total energy  $E_{tot}(t)$  within  
 193 the plate therefore satisfies:

$$194 \quad \overline{E_{tot}(t)} \approx \rho h S \overline{v_z(t)^2}. \quad (14)$$

195 where  $\rho$ ,  $h$  and  $S$  are respectively the plate density, thickness and surface  
 196 and  $\overline{v_z(t)^2}$  is the average of the normal squared vibration speed  $v_z(r, t)^2$  over  
 197 several periods. When the field is diffuse, energy losses due to viscoelastic  
 198 dissipation are proportional to the total energy within the structure:

$$199 \quad \frac{d\overline{E_{tot}(t)}}{dt} \approx -\frac{\overline{E_{tot}(t)}}{\tau}, \quad (15)$$

200 with  $\tau$ , the characteristic time of energy dissipation. In a narrow frequency  
 201 range centered on  $\omega_0$ , this time equals  $(\gamma(\omega_0)v_g(\omega_0))^{-1}$  (see Appendix B).  
 202 As a consequence, the energy decreases exponentially with time:

$$203 \quad \overline{E_{tot}(t)} \approx \overline{E_{tot}(t_0)} \exp\left(-\frac{t - t_0}{\tau}\right), \quad (16)$$

204 where  $t_0$  is the instant of the impact. The elastic energy radiated in the plate  
 205 at the instant  $t_0$  is therefore:

$$206 \quad W_{el} = \overline{E_{tot}(t_0)} \approx \rho h S \overline{v_z(t_0)^2}. \quad (17)$$

207 Knowing the instant of impact  $t_0$  and the characteristic time  $\tau$  is sufficient to  
 208 determine the radiated elastic energy  $W_{el}$ . Note that  $\overline{v_z(t_0)^2}$  may fluctuate  
 209 with the position of vibration measurement depending on how the assembly  
 210 of proper modes of the plate are excited. Equation (17) requires that only one  
 211 mode is excited within the plate because the characteristic time  $\tau$  of energy

212 attenuation depends on the mode. Therefore, we assume that no mode con-  
 213 version occurs off the plate boundaries between the normally vibrating mode  
 214  $A_0$  and transversal horizontal ( $TH$ ) or longitudinal ( $S_0$ ) modes. This hy-  
 215 pothesis is valid provided that the plate boundaries are straight and smooth  
 216 [e.g. 35].

## 217 2.2. Thick blocks

218 A force  $\mathbf{F}(t) = -F_z \mathbf{u}_z$  is applied normally at a given position  $(x, y, 0)$  over  
 219 the surface ( $z = 0$ ) of a homogeneous and isotropic thick block (Figure 3).  
 220 The expression “thick block” means that the duration of impact is shorter  
 221 than the two-way travel time of the compressional wave from the closest side  
 222 of the block.

223 The problem of wave generation in a semi-infinite solid is commonly re-  
 224 ferred as Lamb’s problem [1]. It has been treated many times for various  
 225 sources below the surface [e.g. 1, 3, 38] and at the surface [e.g. 1, 21, 38, 39].  
 226 The elastic energy  $W_{el}$  initially input by a normal surface force within blocks  
 227 is distributed among three different modes: compressional wave  $P$ , shear ver-  
 228 tical wave  $SV$  and surface Rayleigh waves. Sánchez-Sesma et al. [40] give the  
 229 partitions  $\pi_P$ ,  $\pi_S$  and  $\pi_R$  of energy radiated in  $P$ ,  $SV$  and Rayleigh waves  
 230 respectively, as a function of the Poisson ratio  $\nu$ . For a concrete block with  
 231  $\nu = 0.4$ , the energy partition is  $\pi_R \approx 61\%$  in Rayleigh waves,  $\pi_S \approx 35\%$  in  
 232  $SV$  waves and only  $\pi_P \approx 4\%$  in  $P$  waves.

233 The vibration propagating at the surface of the block contains Rayleigh  
 234 waves but also compressional and shear waves as shown by the expression of  
 235 the Green’s function  $\tilde{G}_{zz}$  owing to a normal surface force (Appendix C):

$$236 \quad \tilde{G}_{zz} = \tilde{G}_{zz}^P + \tilde{G}_{zz}^S + \tilde{G}_{zz}^R \quad (18)$$



237 where  $\tilde{G}_{zz}^P$ ,  $\tilde{G}_{zz}^S$  and  $\tilde{G}_{zz}^R$  are the contributions of each mode:

$$238 \quad \tilde{G}_{zz}^P(r, \omega) \approx -\frac{i}{\mu} A_P \frac{k_1}{(k_1 r)^2} \exp(-i\omega r/c_P), \quad (19)$$

$$239 \quad \tilde{G}_{zz}^S(r, \omega) \approx -\frac{i}{\mu} A_S \frac{k_1}{(k_1 r)^2} \exp(-i\omega r/c_S), \quad (20)$$

$$240 \quad \tilde{G}_{zz}^R(r, \omega) \approx -\frac{i}{\mu} A_R k_1 \sqrt{\frac{2}{\pi k_1 r}} \exp\left(-i\left(\omega r/c_R - \frac{\pi}{4}\right)\right). \quad (21)$$

241 In these equations,  $A_P$ ,  $A_S$  and  $A_R$  are functions of Poisson's ratio  $\nu$  (Appendix C),  
 242  $c_P$ ,  $c_S$  and  $c_R$  are the compressional, shear and Rayleigh wave speeds, respec-  
 243 tively,  $\mu$  is the Lamé shear modulus and  $k_1 = \omega/c_P$  is the wave number. The  
 244 expressions of these Green's functions show that the energy of compressional  
 245 and shear waves at the surface decreases with frequency  $f$  and distance  $r$   
 246 as  $(fr)^{-4}$  while the energy of Rayleigh waves varies as  $f/r$  because they are  
 247 guided at the surface. Therefore, the Rayleigh waves dominate the signal at  
 248 high frequencies and far from the impact [1, 21].

249 In the following, we apply the energy flux and deconvolution methods on  
 250 the Rayleigh waves to deduce the absolute radiated elastic energy  $W_{el}$ . Con-  
 251 sequently, we need to determine the percentage  $\pi_R^{\text{surf}}(r)$  of Rayleigh waves in  
 252 the energy at the position  $r$  from the impact. To that end, we compute the  
 253 impact force from Hertz's elastic model [e.g. 30] (Figure 4a) and convolve it  
 254 with the Green's functions  $\tilde{G}_{zz}^P$ ,  $\tilde{G}_{zz}^S$  and  $\tilde{G}_{zz}^R$  and the total Green's function  
 255 at  $r = 20$  cm on concrete (Figure 4b) to obtain the synthetic vibration ac-  
 256 celeration  $a_z(r, t)$  associated with each mode (Figure 4c). The compressional  
 257 wave arrives clearly before the other modes. However, shear and Rayleigh  
 258 waves arrive roughly at the same time and are mixed together. The total  
 259 vibration acceleration  $a_z(r, t)$  is very similar to that of the Rayleigh waves  
 260 with the exception of the small wavelet corresponding to the compressional

261 wave. Because shear and Rayleigh waves are out of phase, the maximum  
 262 amplitude of the total vibration acceleration is 12% lower than that of the  
 263 Rayleigh waves only and its squared integral is 18% lower.

264 The contribution of each mode  $n$  to the signal energy as a function of the  
 265 frequency  $f$  is therefore simply  $|\tilde{A}_z^n(r, f)|^2 / \sum_i |\tilde{A}_z^i(r, f)|^2$ , where  $|\tilde{A}_z^n(r, f)|$  is  
 266 the amplitude spectrum of the signal  $a_z^n(r, t)$  associated with the  $n^{\text{th}}$  mode  
 267 (Figure 4d). Shear waves dominate the signal at low frequencies up to about  
 268  $f = 7000$  Hz, where Rayleigh waves become overriding. The percentage of  
 269 compressional waves is much smaller ( $<10\%$ ) and decreases with frequency.  
 270 For frequencies greater than 30 kHz, the surface vibration contains only  
 271 Rayleigh waves. The integration of these energy partitions over the fre-  
 272 quencies  $f$  gives the percentages of Rayleigh, compressional and shear waves  
 273 at the surface (Figures 4e and 4f). For example, the percentages for a 5 mm  
 274 diameter steel bead dropped from a height of 10 cm at  $r = 20$  cm on a  
 275 concrete block ( $\nu = 0.4$ ) are respectively  $\pi_R^{\text{surf}} = 98.5\%$ ,  $\pi_P^{\text{surf}} = 0.1\%$  and  
 276  $\pi_S^{\text{surf}} = 1.4\%$ . Note that, at a given distance from the impact, the percentage  
 277  $\pi_R^{\text{surf}}$  of Rayleigh waves decreases as the bead diameter  $d$  increases (Figure  
 278 4e) and the height of fall  $H$  decreases (Figure 4f). For example, at  $r = 20$   
 279 cm, Rayleigh waves represent 99.9% of the signal for  $d = 1$  mm while only  
 280 about 71% for  $d = 20$  mm (Figure 4e). In other words, if we assume that the  
 281 signal contains only Rayleigh waves at  $r = 20$  cm from the impact, the error  
 282 introduced in the energy  $W_{el}$  is negligible for a bead of diameter  $d = 1$  mm  
 283 but is about 30% for  $d = 20$  mm. On the other hand, the influence of the  
 284 height of fall  $H$  on this percentage is negligible over the range of heights  
 285 investigated here (5 cm to 50 cm, Figure 4f).

286 For the last method, based on the diffuse field approximation, the parti-  
 287 tions  $\pi_R$  and  $\pi_R^{\text{surf}}(r)$  indicated above are no longer valid because the energy  
 288 is distributed over the three directions of space  $x$ ,  $y$  and  $z$ . In this case, we  
 289 use the horizontal to vertical amplitude ratio

$$290 \quad \left(\frac{\mathcal{H}}{\mathcal{V}}\right)_{\text{diffuse}} = \frac{|\tilde{V}_x(r, \omega)| + |\tilde{V}_y(r, \omega)|}{|\tilde{V}_z(r, \omega)|}, \quad (22)$$

291 calculated by [40] for diffuse fields, to deduce the radiated elastic energy  $W_{el}$   
 292 from the normal surface vibration speed  $\tilde{V}_z(r, \omega)$ , using the same method as  
 293 for plates (see section 2.1.3).

### 294 2.2.1. Energy flux method

295 We can estimate the absolute energy radiated in elastic waves  $W_{el}$  from  
 296 the energy transported by Rayleigh waves. Because Rayleigh waves prop-  
 297 agates radially from the impact location, their energy  $W_{el}^R$  is calculated  
 298 similarly to the radiated elastic energy in plates [equation (7)]:

$$299 \quad W_{el}^R = \frac{1}{\pi} \int_0^{+\infty} \left[ \rho v_g \iint_S |\tilde{V}^R(r, z, \omega)|^2 r d\theta dz \right] d\omega. \quad (23)$$

300 Rayleigh waves have an elliptical motion parallel to the direction of propaga-  
 301 tion and normal to the surface, their vibration speed can therefore be written  
 302  $\tilde{\mathbf{V}}^R = \tilde{V}_r^R \mathbf{u}_r + \tilde{V}_z^R \mathbf{u}_z$  (Figure 3) [e.g. 3]. The asymptotic amplitudes far from  
 303 the source of the vibration speeds  $\tilde{V}_r^R$  and  $\tilde{V}_z^R$  are given as a function of  
 304 depth  $z$  by Miller and Pursey [21]:

$$305 \quad |\tilde{V}_r^R(r, z, \omega)| \approx \omega \frac{\tilde{F}_z(\omega)}{\mu f'_0(x_0)} \sqrt{\frac{\pi k_1 x_0^3}{2r}} \left( 2\sqrt{x_0^2 - 1} \sqrt{x_0^2 - \xi^2} e_\xi - (2x_0^2 - \xi^2) e_1 \right) \quad (24)$$

$$306 \quad |\tilde{V}_z^R(r, z, \omega)| \approx \omega \frac{\tilde{F}_z(\omega)}{\mu f'_0(x_0)} \sqrt{\frac{\pi k_1 x_0 (x_0^2 - 1)}{2r}} \left( 2x_0^2 e_\xi - (2x_0^2 - \xi^2) e_1 \right), \quad (25)$$

307 where  $\mu$  is the Lamé shear modulus,  $k_1 = \omega/c_P$ , with angular frequency  $\omega =$   
308  $2\pi f$  and compressional wave speed  $c_P$ ,  $f_0(x) = (2x^2 - \xi^2)^2 - 4x^2\sqrt{(x^2 - 1)(x^2 - \xi^2)}$ ,  
309  $x_0$  is the positive root of  $f_0$  (Figure 5),  $\xi = \sqrt{2(1 - \nu)/(1 - 2\nu)}$ ,  $\nu$  is Pois-  
310 son's ratio,  $e_\xi = \exp(-k_1 z \sqrt{x_0^2 - \xi^2})$  and  $e_1 = \exp(-k_1 z \sqrt{x_0^2 - 1})$ . From  
311 these equations, we deduce that the total vibration speed  $\tilde{V}^R$  is related to  
312 its vertical component  $\tilde{V}_z^R$  by:

$$313 \quad |\tilde{V}^R(r, z, \omega)|^2 = |\tilde{V}_z^R(r, z, \omega)|^2 \left[ 1 + \left( \frac{\mathcal{H}}{\mathcal{V}} \right)_R^2 \right] \quad (26)$$

314 with

$$315 \quad \left( \frac{\mathcal{H}}{\mathcal{V}} \right)_R = \frac{|V_r^R(r, z, \omega)|}{|V_z^R(r, z, \omega)|} = \frac{x_0}{\sqrt{x_0^2 - 1}} \frac{2\sqrt{x_0^2 - 1}\sqrt{x_0^2 - \xi^2}e_\xi - (2x_0^2 - \xi^2)e_1}{2x_0^2e_\xi - (2x_0^2 - \xi^2)e_1}. \quad (27)$$

316 Equation (25) also shows that  $\tilde{V}_z^R$  decreases exponentially with depth  $z$  as

$$317 \quad \tilde{V}_z^R(r, z, \omega) = \tilde{V}_z^R(r, z = 0, \omega) \frac{2x_0^2e_\xi - (2x_0^2 - \xi^2)e_1}{\xi^2}. \quad (28)$$

318 The integral over the surface  $S$  surrounding the impact in equation (23)  
319 then becomes:

$$320 \quad \iint_S |\tilde{V}^R(r, z, \omega)|^2 r d\theta dz = 2\pi r \frac{|\tilde{V}_z^R(r, z = 0, \omega)|^2}{k_1} A(\nu), \quad (29)$$

321 where  $A(\nu) = \int_0^{+\infty} \left[ 1 + \left( \frac{\mathcal{H}}{\mathcal{V}} \right)_R^2 \right] (2x_0^2e_\xi - (2x_0^2 - \xi^2)e_1)^2 / \xi^4 d(k_1 z)$  is a function  
322 of Poisson's ratio  $\nu$  only and equal to 1.6 for our concrete block with  $\nu = 0.4$ .

323 Furthermore, as discussed earlier, the squared vibration speed of Rayleigh  
324 waves  $|\tilde{V}_z^R(r, z = 0, \omega)|^2$  represents a proportion  $\pi_R^{\text{surf}}(r)$  of the vertical squared  
325 vibration speed  $|\tilde{V}_z(r, z = 0, \omega)|^2$ , that also includes the effects of compres-  
326 sional and shear waves. Thus, using equations (23), (26) and (29), we express

327 the energy  $W_R$  of Rayleigh waves as a function of the sole vertical component  
 328 of the vibration speed measured at the surface of the block:

$$329 \quad W_{el}^R = 2\rho r v_g c_p \pi_R^{\text{surf}}(r) A(\nu) \int_0^{+\infty} |\tilde{V}_z(r, z=0, \omega)|^2 \omega^{-1} \exp(\gamma(\omega)r) d\omega, \quad (30)$$

330 where  $\exp(\gamma(\omega)r)$  counterbalances the viscoelastic dissipation of energy. In  
 331 practice, we cut the frequencies below 3 kHz in the amplitude spectrum  
 332  $|\tilde{V}_z(r, z=0, \omega)|$  to avoid the divergence of the term within the integral as  $\omega$   
 333 tends towards 0 (see section 2.1.2).

334 Finally, the energy  $W_{el}^R$  of Rayleigh waves represents only a percentage  
 335  $\pi_R$  of the total elastic energy  $W_{el}$  radiated within the block, thus:

$$336 \quad W_{el} = \frac{W_{el}^R}{\pi_R} = 2\rho r v_g c_p \frac{\pi_R^{\text{surf}}(r)}{\pi_R} A(\nu) \int_0^{+\infty} |\tilde{V}_z(r, z=0, \omega)|^2 \omega^{-1} \exp(\gamma(\omega)r) d\omega. \quad (31)$$

### 337 2.2.2. Deconvolution method

338 Miller and Pursey [21] deduced an analytical expression for the radiated  
 339 elastic energy  $W_{el}$  from the surface deformation created by the action of a  
 340 point force  $\tilde{F}(\omega)$  (in the time Fourier domain) on the surface of a semi-infinite  
 341 solid, using equation (5):

$$342 \quad W_{el} = \frac{\xi^4 \beta}{2\pi^2 \rho c_p^3} \int_0^{+\infty} \omega^2 |\tilde{F}(\omega)|^2 d\omega, \quad (32)$$

343 where  $\beta$  is the imaginary part of

$$344 \quad \int_0^X \frac{x \sqrt{x^2 - 1}}{f_0(x)} dx, \quad (33)$$

345 with  $f_0(x) = (2x^2 - \xi^2)^2 - 4x^2 \sqrt{(x^2 - 1)(x^2 - \xi^2)}$ ,  $\xi = \sqrt{2(1 - \nu)/(1 - 2\nu)}$   
 346 and  $X$  a number greater than the real root  $x_0$  of  $f_0$ . The coefficient  $\beta$  depends

347 only on the Poisson ratio  $\nu$  (see Appendix D for details on the calculation  
348 of  $\beta$ ).

349 In our case, the impact force  $\tilde{F}(\omega)$  is vertical and can be obtained from the  
350 normal surface vibration speed  $\tilde{V}_z^R(r, z = 0, \omega)$  using equation (11) with the  
351 Green's function of Rayleigh waves [equation (21)]. Therefore, the radiated  
352 elastic energy  $W_{el}$  is given by:

$$353 \quad W_{el} = \frac{\xi^4 \beta \pi_R^{\text{surf}}(r)}{2\pi^2 \rho c_p^3} \int_0^{+\infty} \frac{|\tilde{V}_z^R(r, z = 0, \omega)|^2}{|\tilde{G}_{zz}^R(r, \omega)|^2} \exp(\gamma(\omega)r) d\omega \quad (34)$$

354 To compute the radiated elastic energy, we perform the same operation as  
355 in section 2.1.2 because the inverse Green's function  $1/\tilde{G}_{zz}$  also diverges as  
356  $\omega$  tends toward 0.

357 If we replace  $|\tilde{G}_{zz}^R(r, \omega)|$  by its expression in equation (21), we obtain:

$$358 \quad W_{el} = 2\rho r v_g c_p \pi_R^{\text{surf}}(r) \frac{\beta x_0}{8\pi A_R^2} \int_0^{+\infty} |\tilde{V}_z(r, z = 0, \omega)|^2 \omega^{-1} \exp(\gamma(\omega)r) d\omega \quad (35)$$

359 Note that the energy  $W_{el}$  calculated with the energy flux method [equation  
360 (31)] and the energy calculated from the impact force [equation (35)] are pro-  
361 portional to the same integral. The discrepancy between the energies com-  
362 puted with the two methods can be estimated by the ratio of the coefficients  
363 in front of the integral in equations (31) and (35), i.e.  $\beta x_0 \pi_R / 8\pi A_R^2 A(\nu)$ ,  
364 which equals  $1 \pm 10^{-4}$  regardless of Poisson's ratio  $\nu$ . The two methods are  
365 therefore equivalent.

### 366 2.2.3. Diffuse method

367 After many reflections of the wave front off the block boundaries, we  
368 assume that the energy within the block is distributed along the three direc-  
369 tions of space, i.e. that the field is diffuse [e.g. 25]. The ratio of horizontal

370 to vertical amplitude at the surface of a semi-infinite medium under a dif-  
 371 fuse field approximation is given by Sánchez-Sesma et al. [40] for a normal  
 372 loading force as a function of the Poisson ratio  $\nu$ :  $\left(\frac{\mathcal{H}}{\mathcal{V}}\right)_{\text{diffuse}} \approx 1.245 + 0.348\nu$ .  
 373 For our concrete block ( $\nu = 0.4$ ),  $\left(\frac{\mathcal{H}}{\mathcal{V}}\right)_{\text{diffuse}} \approx 1.38$ . From the hypothesis of  
 374 energy equipartition, we obtain an expression for the radiated elastic energy  
 375  $W_{el}$  that is similar to that previously demonstrated for plates [equation (17)]:

$$376 \quad W \approx \left(1 + \left(\frac{\mathcal{H}}{\mathcal{V}}\right)_{\text{diffuse}}^2\right) \rho V \overline{v_z(t_0)^2}, \quad (36)$$

377 where  $V$  is the block volume. In the case of blocks, the factor  $1 + \left(\frac{\mathcal{H}}{\mathcal{V}}\right)_{\text{diffuse}}^2$   
 378 compensates the energy distribution over the three directions of space.

### 379 **3. Experimental test**

#### 380 *3.1. Setup*

381 We conduct impact experiments on two thin plates and a thick block to  
 382 test the three methods presented in section 2. Piezoelectric charge shock  
 383 accelerometers (type 8309, *Brüel & Kjaer*) record the normal acceleration  
 384 generated by impacts at various positions. The surface vibration is digitalized  
 385 with an acquisition rate of 0.3 MHz. The accelerometers have a rather flat  
 386 response over a wide range of frequencies (1 Hz to 54 kHz). Note that only one  
 387 accelerometer is necessary to measure the radiated elastic energy regardless  
 388 of the method used because the radiated wave field is isotropic. Nevertheless,  
 389 several sensors are placed at different distances from the impact to measure  
 390 wave dispersion (Appendix A) and energy attenuation, i.e. the coefficients  
 391  $\gamma$  and  $\tau$  (Appendix B and Table 2).

392 The impactors are spherical steel beads of density  $7800 \text{ kg m}^{-3}$  and di-  
393 ameter ranging from 1 mm to 20 mm. The beads are dropped from various  
394 heights from 2 cm to 25 cm, without initial velocity and rotation, on a cir-  
395 cular glass plate with a radius of 40 cm and thickness of 1 cm, on a  $1.2 \times 1$   
396  $\text{m}^2$  PMMA plate with a thickness of 1 cm and on a  $3 \times 1.5 \times 0.6 \text{ m}^3$  concrete  
397 block. The properties of these structures are presented in Table 2.

### 398 *3.2. Description of the measured signals*

399 The two plates and the block were selected to check as comprehensively  
400 as possible the assumptions made in the previous section to calculate the  
401 radiated elastic energy. On the one hand, after each bead impact on the  
402 glass plate and on the concrete block, the accelerometers record a long coda  
403 owing to the multiple side reflections off the lateral sides of the structure  
404 (Figure 6a and 7a). In these two structures, there are enough reflections for  
405 a diffuse field to be set up and we can apply the diffuse method to estimate  
406 the radiated elastic energy. However, it is not possible to use this method  
407 on the PMMA plate because side reflections are too attenuated (Figure 8a).  
408 After about 30 side reflections in the glass plate and 10 in the concrete block,  
409 the averaged squared vibration amplitude  $|\overline{a_z(r, t)}|^2$  decreases exponentially  
410 with time, until it reaches the noise level (Figures 6b and 7b). We can thus  
411 estimate the characteristic time  $\tau$  of energy attenuation in these structures  
412 (see Appendix B and Table 2).

413 On the other hand, the two plates and the block are sufficiently large to  
414 record a majority of the first arrival of the emitted vibration before the return  
415 of the first side reflection (Figures 6c, 7c and 8a). We can therefore apply  
416 the methods based on the first arrival i.e., the energy flux and deconvolution



417 methods, to determine the elastic energy radiated by the impacts on each  
418 investigated structure.

419 The time Fourier transform of the first arrival gives the amplitude spec-  
420 trum  $|\tilde{A}_z(r, f)|$  (Figures 6d, 7d and 8c). Impacts of beads excite a wide  
421 frequency range up to about 80 kHz and are characterized by an energy peak  
422 with a central frequency between 2 kHz and 40 kHz (Figure 9). The dura-  
423 tion of impact increases with the bead diameter and consequently the peak  
424 frequency of the generated vibration decreases. Interestingly, for impacts of  
425 beads of diameter smaller than 5 mm on the glass plate, the peak frequency  
426 is constant and equals 34 kHz. This is discussed in section 4.2.

### 427 3.3. Radiated elastic energy

428 For experiments of bead impacts on the glass and PMMA plates, the  
429 energy flux and deconvolution methods give almost identical results (Figure  
430 10a and 10c). The energy obtained with deconvolution is 2% greater than  
431 that obtained with the energy flux method on the glass plate and 5% greater  
432 on PMMA. On the glass plate, we also observe a fair agreement between the  
433 energy estimated using the energy flux method and the diffuse method (Fig-  
434 ure 10b). The lower signal to noise ratio for small beads (i.e. for  $W_{el} < 10^{-7}$   
435 J, Figure 10b) leads to an error of +20% on the radiated elastic energy  $W_{el}$   
436 with the diffuse method with respect to the energy flux method. However,  
437 the discrepancy between the methods is lower than the uncertainties on the  
438 energy  $W_{el}$  ( $\pm 1$  standard deviation). The error is about  $\pm 37\%$  with the en-  
439 ergy flux method,  $\pm 36\%$  with the deconvolution method and  $\pm 53\%$  with the  
440 diffuse method. The error is greater ( $\pm 60\%$ ) for beads smaller than 2 mm  
441 (i.e. for  $W_{el} < 10^{-7}$  J, Figure 10) because of the lower signal to noise ratio.

442 For impacts on the concrete block, the radiated elastic energy  $W_{el}$  ob-  
 443 tained with the deconvolution method is equal to that computed with the  
 444 energy flux method, as discussed in section 2.2.2 (Figure 11a). The energy  
 445 estimation error with these two methods is that of the integral  $\int_0^{+\infty} |\tilde{V}_z(r, z =$   
 446  $0, \omega)|^2 \omega^{-1} \exp(\gamma(\omega)r) d\omega$  in equations (31) and (35) and is about  $\pm 75\%$ . We  
 447 cannot use the diffuse method for beads smaller than 2 mm in diameter  
 448 because not enough side reflections can be recorded. For larger beads, the  
 449 energy measured with the diffuse method is between 0.3 to 3 times that ob-  
 450 tained with the other methods (Figure 11b). Error bars with the diffuse  
 451 method are between  $\pm 70\%$  and  $\pm 300\%$  and are of the same order of magni-  
 452 tude as the difference between the methods.

453 Let us discuss the possible source of errors in our experiments. For the  
 454 energy flux and deconvolution methods, the error bars are greater on the  
 455 block ( $\approx 75\%$ ) than on the plates ( $\approx 36\%$ ). This is probably because we  
 456 can less clearly identify the first emitted wave train from the side reflections  
 457 in the concrete block than in the plates (Figures 6c, 7c and 8b). Moreover,  
 458 the rough surface of the concrete block is a likely cause for greater scattering  
 459 of the results than on the smooth glass and PMMA plates, in particular for  
 460 beads of diameter  $d < 3$  mm for which the depth of penetration into the  
 461 concrete is of the same order of magnitude as the surface roughness. The  
 462 diffuse method is based on statistical assumptions that induce additional  
 463 errors. First, the diffuse regime is reached after at least 30 side reflections  
 464 in the glass plate and 10 in the concrete block. Consequently, if damping  
 465 is important, as it is the case in concrete, the diffuse field is not completely  
 466 set, the exponential decay of the energy is not clear and the characteristic

467 time  $\tau$  of energy dissipation is not well estimated (Figure 7b). The error on  
468  $\tau$  therefore leads to either overestimate or underestimate the radiated elastic  
469 energy. Secondly, an exponential decay of the energy assumes that the energy  
470 dissipation is frequency independent, which is not completely the case here  
471 (Table 2).

### 472 3.4. Elastic transfer efficiency

473 We measure the total energy  $\Delta E_c$  lost by the beads from their vertical  
474 coefficient of restitution  $e$  [e.g. 28, 41]. The proportion of energy radiated in  
475 elastic waves  $W_{el}$  with respect to the lost energy  $\Delta E_c$ , i.e. the elastic transfer  
476 efficiency, increases with bead diameter up to  $d = 5$  mm and decreases for  
477  $d \geq 10$  mm (Figure 12a). The ratio  $W_{el}/\Delta E_c$  does not depend on the fall  
478 height  $H$  for impacts on the PMMA plate and concrete block (Figure 12b).  
479 On the glass plate, for bead diameters  $d$  between 2 mm and 5 mm and  
480 fall heights  $H > 5$  cm, the radiated elastic energy  $W_{el}$  is greater than the  
481 lost energy  $\Delta E_c$ , which is impossible. We will explain this discrepancy in the  
482 discussion section. More energy is converted into elastic waves for impacts on  
483 the glass plate and on the PMMA plate than on the concrete block. Indeed,  
484 the ratio  $W_{el}/\Delta E_c$  is never greater than 2% on the concrete block while on  
485 the PMMA plate, almost all the lost energy is radiated elastically for bead  
486 diameters  $d \geq 5$  mm (Figure 12a), regardless of the fall height  $H$  (Figure  
487 12b).

## 488 4. Discussion

### 489 4.1. Comparison between the different methods

490 It is valid to use the energy flux and deconvolution methods when the  
491 first wave arrival can be discerned from side reflections or when the side re-  
492 flections are very attenuated. The diffuse method is applicable provided that  
493 enough side reflections occur to equipartition the energy. The diffuse method  
494 therefore becomes very efficient in a small structure. Another advantage of  
495 the diffuse method is that there is no assumption on the direction of the  
496 impact force.

497 The three methods can be used with only one sensor to measure the  
498 radiated elastic energy but the precision of the energy estimation can be  
499 enhanced when several sensors are used. For the direct wave methods, the  
500 use of several sensors can take into account an anisotropic emission. For the  
501 diffuse method, it can compensate for a not completely equipartitioned field  
502 because we estimate the averaged value of the energy over the surface of the  
503 structure.

### 504 4.2. Comparison with Hertz's model of elastic impact

505 Impacts of spherical beads on a plane surface are often compared with  
506 Hertz's [29] theory of elastic impact [e.g. 19, 30, 31, 28, 32, 33]. For example,  
507 using equation (5) with an expression of the impact force  $F_z(\mathbf{r}_0, t)$  based on  
508 Hertz's theory, Hunter [32] and Reed [33] estimated the theoretical value  $W_{el}^{th}$   
509 of the elastic energy emitted by beads impacting thick elastic blocks. How-  
510 ever, their approach has never been extended to the case of impacts on thin  
511 plates. Moreover, if inelastic energy dissipation occurs during the impact,

512 the amplitude of the impact force is expected to decrease with respect to  
513 the elastic case [30, 28, 34] and Hertz’s model may overestimate the radiated  
514 elastic energy.

515 To interpret our results, we compare the measured signals and amplitude  
516 spectra with synthetic signals obtained by convolution of the Green’s function  
517 [equations (12) and (18)] with Hertz’s force of elastic impact (Figures 6c, 6d,  
518 7c, 7d, 8b and 8c). Moreover, we also compare the measured radiated elastic  
519 energy  $W_{el}$  with the energy  $W_{el}^{th}$  of the synthetic signal (Figure 13).

520 A good agreement with elastic theory is observed for the PMMA plate  
521 in terms of amplitude and frequencies (Figures 8b and 8c). The measured  
522 radiated energy  $W_{el}$  in PMMA is generally of the same order of magnitude  
523 but smaller than the theoretical one  $W_{el}^{th}$  by up to a factor of 3 (Figures 13a  
524 and 13b). We used a laser Doppler vibrometer to measure the exact vibra-  
525 tion displacement of the glass plate surface after a bead impact (Figure 14).  
526 This reveals that the system constituted by the accelerometer and the glass  
527 plate shows a resonance frequency around 38 kHz. As a consequence, the  
528 accelerometer records a greater amplitude than that of the generated vibra-  
529 tion at frequencies close to 38 kHz (Figure 14). This is clearly visible both  
530 on the temporal signal and amplitude spectrum when we compare them with  
531 their synthetic counterparts (Figures 6c and 6d). Indeed, the measured sig-  
532 nal lasts much longer than the synthetic signal (Figure 6c) and the measured  
533 spectrum has a higher amplitude than the synthetic spectrum around the  
534 resonance frequency (Figure 6d). Because of the resonance, the measured  
535 radiated elastic energy  $W_{el}$  is up to 4 times greater than  $W_{el}^{th}$  for impacts of  
536 beads of diameter  $d < 10$  mm on the glass plate, regardless of the fall height

537  $H$  (Figures 13a and 13b). More importantly,  $W_{el}$  is even greater than the  
538 lost energy  $\Delta E_c$  (Figures 12a and 12b), which is impossible owing to energy  
539 conservation. This resonance seems excited by impacts of beads of diameter  
540  $d \leq 5$  mm because the peak frequency of the amplitude spectrum generated  
541 by the impacts of these beads is constant and equals 34 kHz (Figure 9),  
542 while it should increase for decreasing bead diameter  $d$  [31]. The origin of  
543 this resonance is still under study.

544 It is not clear whether the resonance is also observed for impacts on  
545 the concrete block because the synthetic signal is very different from the  
546 measured signal (Figures 7c and 7d). For example, we can discern the com-  
547 pressional wave and the Rayleigh wave in the synthetic signal but not in  
548 the measured signal (Figure 7c). That said, on concrete, the peak frequency  
549 of the amplitude spectrum decreases for increasing bead diameter  $d$ , which  
550 does not suggest resonance (Figure 9). The measured signal on concrete has  
551 smaller frequencies than the synthetic signal, probably because the duration  
552 of the impact of steel beads on this block is longer than that predicted by  
553 Hertz (Figures 7c and 7d). On the concrete block, the measured radiated  
554 energy  $W_{el}$  is smaller than the theoretical energy  $W_{el}^{th}$  by up to a factor of 7  
555 for bead diameters  $d < 5$  mm and  $d > 10$  mm (Figures 13a and 13b).

556 For impacts on the thin plates, the variation of the energy ratio  $W_{el}/E_c$   
557 with diameter  $d$  is well reproduced by Hertz's theory up to  $d = 10$  mm,  
558 but the agreement is not quantitatively good on the glass plate, probably  
559 due to the resonance (Figures 13c and 13d). For larger beads, however,  
560 Hertz's theory leads to values of the radiated elastic energy  $W_{el}^{th}$  greater than  
561 the impact energy  $E_c$ , which is impossible (Figure 13c). On the concrete

562 block, Hertz's model fails to reproduce the variation of the ratio  $W_{el}/E_c$   
 563 with bead diameter  $d$  (Figure 13c). Indeed, for an elastic impact, the ratio  
 564  $W_{el}^{th}/E_c$  is independent of the bead diameter  $d$  while the measured ratio  
 565  $W_{el}/E_c$  first increases, reaches a maximum for  $d = 5$  mm and then decreases  
 566 (Figure 13c). Similarly, the measured ratio  $W_{el}/E_c$  is roughly independent  
 567 of the fall height  $H$  while theory predicts it should increase (Figure 13d).  
 568 The average measured ratio  $W_{el}/E_c$  on the block is between 0.1% and 2%,  
 569 which is in agreement with previous bead-drop experiments on thick blocks  
 570 [32, 33, 34]. This is however several orders of magnitude higher than the  
 571 ratios  $W_{el}/E_c = 10^{-5}$  to  $10^{-3}$  measured for rockfalls in the field, for which  
 572 plastic deformation is much more important [9, 10].

573 To sum up, it is valid to use Hertz's force of elastic impact to qualitatively  
 574 predict the variation of the radiated elastic energy  $W_{el}$  with bead diameter  
 575  $d$  and fall height  $H$  on a smooth plate when the bead diameter  $d$  is smaller  
 576 than the plate thickness  $h$ . However, the small ratio of  $W_{el}$  to the lost energy  
 577  $\Delta E_c$  for beads of diameter  $d < 3$  mm and  $d > 10$  mm suggests that our  
 578 experiments involve a range of bead diameters and impact speeds in which  
 579 viscoelastic and plastic dissipation may occur (Figure 12a). Hertz's model  
 580 does not take into account inelastic dissipation during impact, which can  
 581 reduce the amplitude of the impact force and thereby decrease the amount  
 582 of energy radiated by elastic waves [see 30]. The difference observed between  
 583 the measured radiated elastic energy  $W_{el}$  and that predicted by Hertz's model  
 584  $W_{el}^{th}$  can therefore be partly explained by the presence of inelastic dissipation.  
 585 A more complex model is therefore needed to account for these energy losses,  
 586 as discussed in the next paragraph.

587 *4.3. Inelastic energy dissipation*

588 For a viscoelastic impact, Ramírez et al. [42] showed that the coefficient  
589 of restitution  $e$  decreases with the impact speed  $V_z$  as  $1 - cV_z^{1/5}$  where  $c$  is  
590 a constant depending on bead diameter. This scaling law agrees well with  
591 our experimental results on the glass and PMMA plates but not with those  
592 on the concrete block (Figure 15). Some energy may therefore be dissipated  
593 viscoelastically on plates. Although not explicitly indicated by the authors,  
594 the model of Ramírez et al. [42] shows that the energy lost by viscoelastic  
595 dissipation is greater for small beads. This is in agreement with our data  
596 because the discrepancy between the measured and the theoretical energy  
597 is larger as the bead diameter  $d$  decreases (Figure 12a). Additional energy  
598 losses may also occur for the smallest beads investigated ( $d < 3$  mm) due  
599 to surface imperfections and adhesion [31]. These effects are even greater on  
600 the concrete block with its surface roughness of  $\approx 0.5$ – $1$  mm. Therefore, the  
601 energy that is not radiated in elastic waves for beads of diameter  $d < 5$  mm  
602 is likely dissipated in viscoelasticity as well as in adhesion and rotational  
603 and translational modes. On the PMMA plate, this inelastic dissipation  
604 represents from 99% to 10% of the lost energy with increasing diameter  $d$   
605 from 1 mm to 4 mm (Figure 12a). On the concrete block, this represents  
606 almost all the lost energy because the percentage of lost energy radiated in  
607 elastic waves is very small (0.1%-2%) (Figure 12a).

608 The minimum impact speed necessary to deform a structure plastically  
609 is very low ( $\simeq 0.1$  m s<sup>-1</sup> for steel impacting steel [30]) and this velocity  
610 is clearly exceeded in all our experiments. However, the minimum impact  
611 speed to cause fully plastic deformation is much higher and such impacts



612 are characterized by a coefficient of restitution  $e$  that decreases with impact  
 613 speed as  $V_z^{-1/4}$  [30]. Our data do not fit this scaling law, even for the largest  
 614 beads investigated (Figure 15). The impacts in our experiments are therefore  
 615 elastic-plastic but not fully plastic. Plastic deformation is more likely to  
 616 occur for the largest beads because higher stresses are developed during the  
 617 impact. As a matter of fact, plastic deformation is evidenced on glass and  
 618 concrete, but not on PMMA, by the presence of small indentations on the  
 619 surface after impacts of beads larger than 10 mm. As a consequence, the  
 620 elastic transfer efficiency decreases for beads of diameter  $d > 5$  mm (Figure  
 621 12a). For a given bead diameter  $d > 10$  mm, the impact seems more elastic  
 622 on PMMA than on glass or on concrete because the ratio  $W_{el}/\Delta E_c$  decreases  
 623 less on PMMA than on the other structures (Figure 12a). As suggested by  
 624 McLaskey and Glaser [31], PMMA is a more compliant material than glass  
 625 and concrete and thereby the impacts lasts longer and over a larger area  
 626 of contact, reducing the maximum stresses applied on the surface. On the  
 627 plates, we estimate that the plastic deformation represents up to 20% of the  
 628 lost energy for  $d = 20$  mm (Figure 12a). This is however not quantifiable on  
 629 the concrete block because the surface roughness may contribute to a high  
 630 proportion of the energy losses.

631 Finally, note that even when inelastic dissipation occurs, the three meth-  
 632 ods of energy calculation compared in this paper give very similar results  
 633 (Figures 10 and 11). However, plastic deformation (or surface roughness)  
 634 may generate an impact force with a greater tangential component, as sug-  
 635 gested by Buttle and Scruby [18]. This can therefore affect our estimation of  
 636 the radiated elastic energy because we make the assumption that the impact

637 force is normal to the surface. For example, Sánchez-Sesma et al. [40] showed  
638 that the stronger the tangential force is on the surface of a semi-infinite block,  
639 the smaller the generated vertical displacement is with respect to the radial  
640 displacement.

## 641 5. Conclusions

642 We presented and validated experimentally three methods to estimate  
643 the elastic energy radiated by an impact on a thin plate and a thick block  
644 from the measurement of the surface normal vibration at a single location.  
645 The energy flux method and deconvolution methods are based on the direct  
646 wave between the impact and are shown to give the same results for both  
647 plates and blocks. The diffuse method makes use of the diffuse coda during  
648 which multiple reflections occur off the structure's borders. This last method  
649 slightly overestimates the radiated elastic energy with respect to the other  
650 methods on plates (+5–20%), but gives results of the same order of magni-  
651 tude (i.e. within a factor of 3) as the other methods when applied to blocks.  
652 The differences between the estimates are however less than the uncertainty  
653 of each method, with standard deviations between 40% and 70% for the en-  
654 ergy flux and deconvolution methods and between 50% and 300% for the  
655 diffuse method.

656 The presented methods have the major advantage of estimating the radi-  
657 ated elastic energy independently with respect to the other energy dissipation  
658 processes, without knowledge of the impact force. This allowed us to estab-  
659 lish an energy budget for the impacts:

- 660 • On thin plates, the percentage of energy lost in elastic waves increases  
661 with the bead diameter. This percentage is less than 2% of the total  
662 energy lost when the bead diameter is smaller than 10% of the plate  
663 thickness. The rest of the energy lost by the bead is likely dissipated by  
664 viscoelasticity. On the other hand, almost all the lost energy is radiated  
665 in elastic waves for bead diameters greater than the plate thickness and

666 the rest is lost in plastic deformation (up to 20% in our experiments).

- 667 • On rough thick blocks, the radiated elastic energy represents only be-  
668 tween 0.2% to 2% of the lost energy, regardless of the bead diameter and  
669 fall height. Inelastic dissipation (i.e. viscoelastic, plastic, rotational,...)  
670 is therefore the major energy consumption process.

671 The elastic impact model of Hertz well reproduces the measured radi-  
672 ated elastic energy on thin plates for bead diameters smaller than the plate  
673 thickness, but overestimates the energy for larger beads. On thick blocks,  
674 the model gives quantitatively good results but overestimates the radiated  
675 elastic energy by a factor of 2 to 10 when inelastic dissipation occurs.

676 Further work is required to investigate how surface roughness affects the  
677 amount of energy radiated in elastic waves and dissipated by inelastic pro-  
678 cesses during an impact. For example, it would be interesting to establish  
679 the energy budget of beads impacts on thick blocks with a surface as smooth  
680 as that of the thin plates.

## 681 **Acknowledgements**

682 We thank V. Farra, J.P. Montagner, E. Stutzmann, R. Madariaga, E.  
683 Falcon, D. Royer, A. Schubnel, T. Reuschl and L. Jouniaux for helpful dis-  
684 cussions. We are indebted to J. Martin for his useful pieces of advice in signal  
685 processing and to A. Steyer for technical help. We thank the journal editor  
686 Ines Lopez Arteaga and two anonymous reviewers for their helpful com-  
687 ments to increases the clarity of our manuscript. This work was supported  
688 by the european project ERC SLIDEQUAKES, the Agence Nationale de la

689 Recherche ANR LANDQUAKES project, the REALISE project and the ITN  
690 FLOWTRANS project.

691 **Appendix A. Experimental determination of the relations of dis-**  
692 **persion**

693 In this section, we detail how to determine the relations of dispersion  
694 of the structures used for impacts experiments. In order to observe wave  
695 dispersion, we measure the emitted wave front at several distances  $r$  from  
696 a given bead impact (e.g. for PMMA, Figure 16a). The double Fourier  
697 transform in time and space of the vibration acceleration  $a_z(r, t)$  allows to  
698 deduce the relation between the angular frequency  $\omega$  and the wave number  
699  $k$ , i.e. the dispersion relation (Figures 16b and 16c).

700 As expected, for the plates of PMMA and glass the dispersion relation  
701 corresponds exactly to that of the fundamental mode  $A_0$  of Lamb (Figures  
702 16c and 17a). At low frequencies, i.e. for  $kh < 1$ , the dispersion relation  
703 can be approximated by  $\omega \approx 5.5k^2$  in PMMA and  $\omega \approx 13.8k^2$  in glass, thus  
704 satisfying equation (1) with a bending stiffness  $B = 357$  J and  $B = 4760$   
705 J, respectively. On the other hand, the mode  $A_0$  is not dispersive at higher  
706 frequencies, for  $kh > 1$ . Indeed, the relation between the frequency and the  
707 wave number becomes roughly linear and the group velocity  $v_g = \partial\omega/\partial k$   
708 tends towards the Rayleigh wave velocity that is  $\approx 1400$  m s<sup>-1</sup> for PMMA  
709 and  $\approx 3100$  m s<sup>-1</sup> for glass [35].

710 For the glass and PMMA plates, we estimate the energy associated with  
711 the longitudinal  $S_0$  mode with an accelerometer on the plate border. In  
712 both plates, the energy of this mode is about 0.2% of that of the vertical  
713  $A_0$  mode and is consequently negligible. The plates vibration is therefore  
714 mostly normal to the surface. The lowest secondary mode in plates is the  
715 mode  $A_1$  that has a cutoff frequency equal to  $c_S/4h \approx 82$  kHz in glass and

716 22 kHz in PMMA, where  $c_S$  is the shear wave speed. The accelerometers  
717 record frequencies up to 80 kHz, therefore we do not measure modes higher  
718 than the  $A_0$  mode in glass. In PMMA, however, the mode  $A_1$  may be present  
719 but its amplitude is too low to be detected in the dispersion curve  $\omega = f(k)$   
720 (Figure 16c).

721 For the concrete block, the relation between the angular frequency  $\omega$   
722 and the wave number  $k$  is roughly linear with a slope of  $1530 \text{ m s}^{-1}$  that  
723 corresponds to both the phase  $v_\phi$  and group  $v_g$  velocities (Figure 17b).

724 **Appendix B. Energy dissipation model in a viscoelastic solid**

725 In this Appendix, we show that the viscous dissipation of energy with  
 726 distance  $r$  in a Kelvin-Voigt viscoelastic solid can be modeled by a factor  
 727  $\exp(-\gamma r)$  where  $1/\gamma$  is a characteristic length of energy dissipation that de-  
 728 pends on frequency. To that end, we have to demonstrate the equation of  
 729 energy conservation in such a solid. We start from the equation of momentum  
 730 conservation in the solid, stating that:

$$731 \quad \rho \frac{\partial^2 u_i}{\partial t^2} = \frac{\partial T_{ij}}{\partial x_j}, \quad (\text{B.1})$$

732 where  $u_i$  is the wave displacement and  $T_{ij}$  is the stress tensor. The summation  
 733 on repeated indices is implicit. In a homogeneous and isotropic viscoelastic  
 734 solid modeled by Kelvin-Voigt model, Hooke's law is [35]:

$$735 \quad T_{ij} = T_{ij}^{el} + T_{ij}^{inel}, \quad (\text{B.2})$$

736 with

$$737 \quad T_{ij}^{el} = \lambda \delta_{ij} S + 2\mu S_{ij}, \quad (\text{B.3})$$

738 and

$$739 \quad T_{ij}^{inel} = \chi \delta_{ij} \frac{\partial S}{\partial t} + 2\eta \frac{\partial S_{ij}}{\partial t}, \quad (\text{B.4})$$

740 where  $S_{ij} = \frac{1}{2} \left( \frac{\partial u_i}{\partial x_j} + \frac{\partial u_j}{\partial x_i} \right)$  is the strain tensor and  $S = \partial u_j / \partial x_j$ . The con-  
 741 stants  $\lambda$ ,  $\mu$  and  $\chi$ ,  $\eta$  are the elastic and viscous coefficients associated to  
 742 compression and shear, respectively. Note that these coefficients generally  
 743 depend on frequency  $f$ .

744 Multiplying equation (B.1) by  $\frac{\partial u_i}{\partial t}$ , we obtain:

$$745 \quad \frac{\partial e_c}{\partial t} = \frac{\partial T_{ij}^{el}}{\partial x_j} \frac{\partial u_i}{\partial t} + \frac{\partial T_{ij}^{inel}}{\partial x_j} \frac{\partial u_i}{\partial t}, \quad (\text{B.5})$$



746 where  $e_c$  is the bulk density of kinetic energy.

747 We can develop the second term of equation (B.5) noting that:

$$748 \quad \frac{\partial T_{ij}^{el}}{\partial x_j} \frac{\partial u_i}{\partial t} = \frac{\partial}{\partial x_j} \left( T_{ij}^{el} \frac{\partial u_i}{\partial t} \right) - T_{ij}^{el} \frac{\partial^2 u_i}{\partial t \partial x_j}, \quad (\text{B.6})$$

749 According to Royer and Dieulesaint [35], the Poynting vector is defined  
750 by:

$$751 \quad P_j = -T_{ij}^{el} \frac{\partial u_i}{\partial t}. \quad (\text{B.7})$$

752 and verifies, for guided waves:

$$753 \quad \frac{\partial P_j}{\partial x_j} = c_j \frac{\partial e_{tot}}{\partial x_j}, \quad (\text{B.8})$$

754 where  $c_j$  is the energy speed, i.e. the group velocity, in the direction  $\mathbf{x}_j$   
755 and  $e_{tot} = e_c + e_p$  is the bulk density of total energy within the structure.  
756 Moreover, because of the symmetry  $S_{ij} = S_{ji}$  of the strain tensor, we can  
757 show that:

$$758 \quad T_{ij}^{el} \frac{\partial^2 u_i}{\partial t \partial x_j} = \frac{1}{2} (\lambda \delta_{ij} + 2\mu) \frac{\partial}{\partial t} \left( \frac{\partial u_i}{\partial x_j} \frac{\partial u_j}{\partial x_i} \right), \quad (\text{B.9})$$

759 which is the derivative of the bulk density of potential energy  $e_p$ .

760 Injecting equations (B.6), (B.8) and (B.9) in equation (B.5), we obtain:

$$761 \quad \frac{\partial e_{tot}}{\partial t} + c_j \frac{\partial e_{tot}}{\partial x_j} = \frac{\partial T_{ij}^{inel}}{\partial x_j} \frac{\partial u_i}{\partial t}, \quad (\text{B.10})$$

762 where the last term can be developed using equation (B.4).

763 If we assume that the wave is longitudinal and propagates in direction  $\mathbf{x}_1$   
764 ( $u_2 = 0$ ), the wave displacement is:

$$765 \quad u_1 = A_1 \sin(\omega(t - x_1/c_P)), \quad (\text{B.11})$$

766 where  $A_1$  is the amplitude,  $\omega$  is the angular frequency and  $c_P$  is the com-  
 767 pressional wave speed. Thus we get:

$$768 \quad \frac{\partial T_{ij}^{inel}}{\partial x_j} \frac{\partial u_i}{\partial t} = -(\chi + 2\eta) A_1^2 \frac{\omega^4}{c_P^2} \cos^2(\omega(t - x_1/c_P)). \quad (\text{B.12})$$

769 If we remark that the bulk density of energy  $e_{tot}$  is equal to

$$770 \quad \rho \left( \frac{\partial u_1}{\partial t} \right)^2 = \rho \omega^2 A_1^2 \cos^2(\omega(t - x_1/c_P)), \quad (\text{B.13})$$

771 we obtain:

$$772 \quad \frac{\partial T_{ij}^{inel}}{\partial x_j} \frac{\partial u_i}{\partial t} = -(\chi + 2\eta) \frac{\omega^2}{\rho c_P^2} e_{tot}. \quad (\text{B.14})$$

773 Using equations (B.10) and (B.14), we have finally demonstrated that  
 774 the equation of energy conservation of a longitudinal wave propagating in a  
 775 viscoelastic solid is:

$$776 \quad \frac{\partial e_{tot}}{\partial t} + \mathbf{v}_g \cdot \nabla e_{tot} = -\frac{e_{tot}}{\tau}, \quad (\text{B.15})$$

777 with  $v_g = c_P$ , the group speed and  $\tau$ , the characteristic time of energy  
 778 dissipation [see e.g. 35, 43]:

$$779 \quad \tau = \frac{\rho c_P^2}{(\chi + 2\eta)\omega^2} = \frac{1}{\gamma v_g}. \quad (\text{B.16})$$

780 In equation (B.15), the term  $-e_{tot}/\tau$  represents energy dissipation with  
 781 time when the source force is not acting on the structure any more [e.g. 36].

782 Multiplying this equation by  $\exp(t/\tau)$  gives:

$$783 \quad \left( \frac{\partial e_{tot}}{\partial t} + \frac{e_{tot}}{\tau} \right) \exp\left(\frac{t}{\tau}\right) + \mathbf{v}_g \cdot \nabla e_{tot} \exp\left(\frac{t}{\tau}\right) = 0. \quad (\text{B.17})$$

784 Writing  $e'_{tot} = e_{tot} \exp(t/\tau)$  leads to:

$$785 \quad \frac{\partial e'_{tot}}{\partial t} + \mathbf{v}_g \cdot \nabla e'_{tot} = 0 \quad (\text{B.18})$$

786 Thus energy  $e'_{tot} = e_{tot} \exp(t/\tau) = e_{tot} \exp(\gamma r)$  is conserved. Therefore, mul-  
 787 tiplying the energy by the factor  $\exp(\gamma r)$  compensates the viscoelastic dissi-  
 788 pation of energy with distance.

789 Note that if the wave is transversal and polarized along direction  $\mathbf{x}_2$  and  
 790 propagates along direction  $\mathbf{x}_1$ , we have:

$$791 \quad \frac{\partial T_{ij}^{inel}}{\partial x_j} \frac{\partial u_i}{\partial t} = -\eta A_2^2 \frac{\omega^4}{c_S^2} \cos^2(\omega(t - x_2/c_S)), \quad (\text{B.19})$$

792 and we retrieve the conservation equation (B.15) with a different coefficient  
 793  $\tau = \rho c_S^2 / \eta \omega^2$ , with  $c_S$ , the shear wave speed. Practically, the waves propagat-  
 794 ing in thin plates and thick blocks are a complex combination of longitudi-  
 795 nal and transversal waves. If we consider only one of these modes, either the  
 796 mode  $A_0$  of Lamb or the Rayleigh waves, the equation (B.15) of energy con-  
 797 servation is still verified provided that we integrate it over the depth [35] but  
 798 the expression of the characteristic coefficient  $\tau$  is much more complicated.

799 Here, we validate experimentally the model of energy attenuation in  
 800  $\exp(-t/\tau)$  or in  $\exp(-\gamma r)$  in the thin plates and the thick block investi-  
 801 gated. To do so, we estimate the coefficient  $\gamma$  by measuring the first arrival  
 802 of the emitted vibration at different distances  $r$  from an impact (Figure 18a)  
 803 and filtering this vibration in different frequency ranges. For example in the  
 804 PMMA plate, the squared amplitude of the  $A_0$  mode decreases with distance  
 805  $r$  as  $\frac{1}{r} \exp(-\gamma r)$  (Figures 18b to 18d). We deduce the value of  $\gamma$  as a function  
 806 of frequency  $f$  (Figure 18e).

807 When the first arrival can not be separated from the side reflections or  
 808 when numerous side reflections occur in the structure after an impact, we  
 809 can determine energy attenuation with an other method. For example on  
 810 the glass plate, after an impact the envelope of the squared signal averaged

811 over several periods decreases exponentially with time as:

$$812 \quad \overline{A(t)^2} = \overline{A(t=0)^2} \exp\left(-\frac{t}{\tau}\right), \quad (\text{B.20})$$

813 where  $t = 0$  is the impact time (Figure 19a). The characteristic time  $\tau$  at  
814 frequency  $f$  is simply the inverse of the slope of  $\overline{A(t)^2}$  in semi-log scale, filtered  
815 in a frequency range centered on  $f$  (Figures 19b to 19d). We thus show how  
816 the characteristic time  $\tau$  decreases as the frequency  $f$  increases (Figure 19e).  
817 Note that for a diffuse field, the inverse of  $\tau$  is given by the average of the  
818 inverse of the characteristic times  $\tau$  of each modes of propagation weighed  
819 by their percentage of partition.

820 **Appendix C. Green's functions owing to a vertical load at the**  
821 **surface of an elastic half-space**

822 Here we recall the expression of the time Fourier's transform of the  
823 Green's function  $\tilde{G}_{zz}(r, \omega)$  at the surface of a half-space owing to a verti-  
824 cal load on the surface.

825 Miller and Pursey [38] determined the exact expression of the surface  
826 vertical displacements  $\tilde{U}_z(r, z, \omega)$  generated at a distance  $r$  by a normal force  
827  $\mathbf{F} = \tilde{F}_z(\omega)\mathbf{u}_z$  on the surface of an elastic half-space [equation (72) of their  
828 paper with  $z = 0$ ]:

$$829 \quad \tilde{U}_z(r, \omega) = \frac{\tilde{F}_z(\omega)\xi^2}{\pi a\mu} \int_0^{+\infty} \frac{\sqrt{x^2 - 1}}{f_0(x)} J_1(k_1 ax) J_0(k_1 rx) dx, \quad (\text{C.1})$$

830 where  $a$  is the radius of the loading area,  $\mu$  the Lamé shear modulus,  $k_1 =$   
831  $\omega/c_P$ , with the angular frequency  $\omega = 2\pi f$  and the compressional wave speed  
832  $c_P$ ,  $f_0(x) = (2x^2 - \xi^2)^2 - 4x^2\sqrt{(x^2 - 1)(x^2 - \xi^2)}$ ,  $\xi = \sqrt{2(1 - \nu)/(1 - 2\nu)}$  and  
833  $\nu$  is Poisson's ratio.  $J_0$  and  $J_1$  are the Bessel's functions of the first kind.

834 For very small values of the radius of contact  $a$ ,  $J_1(k_1 ax)$  can be approx-  
835 imated at a first order by  $k_1 ax/2 + O(a^2)$  so that

$$836 \quad \tilde{U}_z(r, \omega) \approx \frac{\tilde{F}_z(\omega)\xi^2}{2\pi\mu} k_1 \int_0^{+\infty} \frac{x\sqrt{x^2 - 1}}{f_0(x)} J_0(k_1 rx) dx. \quad (\text{C.2})$$

837 A first order approximation of the integral in equation (C.2) was calcu-  
838 lated by Miller and Pursey [21] for large values of  $k_1 r = 2\pi fr/c_P$ . From  
839 a practical viewpoint, this approximation is valid for impact problems be-  
840 cause the impact generates high frequencies  $1 \text{ kHz} < f < 80 \text{ kHz}$  (Figures  
841 6d, 8c and 7d) and  $k_1 r \gg 1$  even for small distances  $r$  from the impact  
842 location. Using this computation, we can show that the vertical Green's

843 function  $\tilde{G}_{zz}(r, \omega) = \tilde{U}_z(r, \omega)/\tilde{F}_z(\omega)$  is the sum of contributions of compres-  
 844 sional, shear and Rayleigh waves, respectively,  $\tilde{G}_{zz}^P$ ,  $\tilde{G}_{zz}^S$  and  $\tilde{G}_{zz}^R$ :

$$845 \quad \tilde{G}_{zz} = \tilde{G}_{zz}^P + \tilde{G}_{zz}^S + \tilde{G}_{zz}^R \quad (\text{C.3})$$

846 with

$$847 \quad \tilde{G}_{zz}^P(r, \omega) \approx -\frac{i}{\mu} A_P \frac{k_1}{(k_1 r)^2} \exp(-i\omega r/c_P), \quad (\text{C.4})$$

$$848 \quad \tilde{G}_{zz}^S(r, \omega) \approx -\frac{i}{\mu} A_S \frac{k_1}{(k_1 r)^2} \exp(-i\omega r/c_S), \quad (\text{C.5})$$

$$849 \quad \tilde{G}_{zz}^R(r, \omega) \approx -\frac{i}{\mu} A_R k_1 \sqrt{\frac{2}{\pi k_1 r}} \exp\left(-i(\omega r/c_R - \frac{\pi}{4})\right), \quad (\text{C.6})$$

850 where  $c_P$ ,  $c_S$  and  $c_R$  are the compressional, shear and Rayleigh waves speeds,  
 851 respectively, and where  $A_P$ ,  $A_S$  and  $A_R$  are only functions of Poisson's ratio  
 852  $\nu$  (Figure 20):

$$853 \quad A_P(\nu) = \frac{\xi^2}{2\pi(2 - \xi^2)^2}, \quad (\text{C.7})$$

$$854 \quad A_S(\nu) = \frac{2(\xi^2 - 1)}{\pi\xi^3}, \quad (\text{C.8})$$

$$855 \quad A_R(\nu) = \frac{\xi^2 \sqrt{x_0(x_0^2 - 1)}}{2 f_0'(x_0)}, \quad (\text{C.9})$$

856 with  $x_0$ , the real positive root of  $f_0(x)$ .

857 **Appendix D. Detailed calculation of coefficient  $\beta$**

858 We detail here the calculation of the coefficient  $\beta$  that appears in the  
 859 expression of the elastic energy  $W_{el}$  radiated in a block [equation (35)].  $\beta$  is  
 860 defined as the imaginary part of

$$861 \int_0^X \frac{x\sqrt{x^2-1}}{f_0(x)} dx, \quad (D.1)$$

862 where  $f_0(x) = (2x^2 - \xi^2)^2 - 4x^2\sqrt{(x^2-1)(x^2-\xi^2)}$ ,  $\xi = \sqrt{2(1-\nu)/(1-2\nu)}$   
 863 and  $\nu$  the Poisson ratio of the block.  $X$  is a number greater than the real  
 864 root  $x_0$  of  $f_0$ , which is represented in Figure 5.

865 Let the function  $f$  be:

$$866 f : x \longrightarrow \frac{x\sqrt{x^2-1}}{(2x^2 - \xi^2)^2 - 4x^2\sqrt{(x^2-1)(x^2-\xi^2)}}. \quad (D.2)$$

867 For most materials, the Poisson ratio  $\nu$  is between 0 and 0.5, correspond-  
 868 ing to values of  $\xi$  from 1.4 to 10. To calculate  $\beta$  we have to look at the  
 869 definition of  $f$  over the intervals  $[0, 1[$ ,  $[1, \xi[$  and  $x \geq \xi$ :

- 870 • For  $x \in [0, 1[$ ,  $x^2 - 1 < 0$  and  $x^2 - \xi^2 < 0$ , then we can then write  
 871  $\sqrt{x^2-1} = i\sqrt{1-x^2}$  and  $\sqrt{x^2-\xi^2} = i\sqrt{\xi^2-x^2}$  where  $i$  is the complex  
 872 number  $\sqrt{-1}$ . Over this interval,  $f(x)$  is a pure imaginary number:

$$873 f(x) = \frac{ix\sqrt{1-x^2}}{(2x^2 - \xi^2)^2 + 4x^2\sqrt{(1-x^2)(\xi^2-x^2)}} \quad (D.3)$$

874 and

$$875 \text{Im}(f(x)) = f_1(x) = \frac{x\sqrt{1-x^2}}{(2x^2 - \xi^2)^2 + 4x^2\sqrt{(1-x^2)(\xi^2-x^2)}}. \quad (D.4)$$

876 Regardless of the value of  $\xi$ ,  $f_1$  is continuous over  $[0, 1]$  with  $f_1(0) =$   
 877  $f_1(1) = 0$  and  $f_1$  is  $C^\infty$  over  $[0, 1[$ .

- 878 • For  $x \in [1, \xi[$ ,  $x^2 - 1 > 0$  and  $x^2 - \xi^2 < 0$ , therefore  $\sqrt{x^2 - \xi^2} =$   
 879  $i\sqrt{\xi^2 - x^2}$ . Over this interval:

$$880 \quad f(x) = \frac{x\sqrt{x^2 - 1}}{(2x^2 - \xi^2)^2 - 4ix^2\sqrt{(x^2 - 1)(\xi^2 - x^2)}}. \quad (\text{D.5})$$

881 Multiplying the numerator and the denominator by the complex con-  
 882 jugate of the denominator leads to:

$$883 \quad f(x) = \frac{x\sqrt{x^2 - 1} \left[ (2x^2 - \xi^2)^2 + 4ix^2\sqrt{(x^2 - 1)(\xi^2 - x^2)} \right]}{(2x^2 - \xi^2)^4 + 16x^4(x^2 - 1)(\xi^2 - x^2)} \quad (\text{D.6})$$

884 and

$$885 \quad \text{Im}(f(x)) = f_2(x) = \frac{4x^3(x^2 - 1)\sqrt{\xi^2 - x^2}}{(2x^2 - \xi^2)^4 + 16x^4(x^2 - 1)(\xi^2 - x^2)}. \quad (\text{D.7})$$

886 Regardless of the value of  $\xi$ ,  $f_2$  is continuous over  $[1, \xi]$  with  $f_2(1) =$   
 887  $f_2(\xi) = 0$  and  $f_2$  is  $C^\infty$  function over  $[1, \xi]$ .

- 888 • For  $x \geq \xi$ ,  $x^2 - 1 > 0$  and  $x^2 - \xi^2 > 0$ , therefore  $f$  is a real function over  
 889 this interval and its imaginary part is null, except for the contribution  
 890 of the pole  $x_0$  of  $f_0$ , which is always greater than  $\xi$  (Figure 5). The  
 891 integral of  $f$  over this interval is due to half of its residue in  $x_0$ :

$$892 \quad \int_{\xi}^X f(x)dx = -i\pi \frac{x_0\sqrt{x_0^2 - 1}}{f_0'(x_0)}. \quad (\text{D.8})$$

893 Finally,  $\beta = \int_0^1 f_1(x)dx + \int_1^{\xi} f_2(x)dx - \pi \frac{x_0\sqrt{x_0^2 - 1}}{f_0'(x_0)}$ .  $\beta$  is represented as a  
 894 function of the Poisson ratio  $\nu$  in Figure 21.



895 **References**

- 896 [1] H. Lamb, On the propagation of tremors over the surface  
897 of an elastic solid, *Philos. T Roy. Soc. A* 203 (1904) 1–42.  
898 doi:10.1098/rsta.1904.0013.
- 899 [2] H. Kanamori, The energy release in great earthquakes, *J. Geophys. Res.*  
900 82 (1977) 2981–2987. doi:10.1029/JB082i020p02981.
- 901 [3] K. Aki, P. Richards, *Quantitative Seismology : Theory and Methods*,  
902 volume 1, W.H. Freeman, 1980.
- 903 [4] X. Pérez-Campos, G. C. Beroza, An apparent mechanism dependence  
904 of radiated seismic energy, *J. Geophys. Res.* 106 (2001) 11127–11136.  
905 doi:10.1029/2000JB900455.
- 906 [5] M. Lancieri, R. Madariaga, F. Bonilla, Spectral scaling of the aftershocks  
907 of the Tocopilla 2007 earthquake in northern Chile, *Geophys. J. Int.* 189  
908 (2012) 469–480. doi:10.1111/j.1365-246X.2011.05327.x.
- 909 [6] J. B. Fletcher, A. McGarr, Moments, magnitudes, and radiated en-  
910 ergies of non-volcanic tremor near Cholame, CA, from ground mo-  
911 tion spectra at UPSAR, *Geophys. Res. Lett.* 38 (2011) L16314.  
912 doi:10.1029/2011GL048636.
- 913 [7] J. Deparis, D. Jongmans, F. Cotton, L. Baillet, F. Thouvenot,  
914 D. Hantz, Analysis of rock-fall and rock-fall avalanche seismograms  
915 in the French Alps, *Bull. Seism. Soc. Am.* 98 (2008) 1781–1796.  
916 doi:10.1785/0120070082.

- 917 [8] I. Vilajosana, E. Suriñach, A. Abellan, G. Khazaradze, D. Garcia,  
918 J. Llosa, Rockfall induced seismic signals: case study in Montser-  
919 rat, Catalonia, *Nat. Hazards Earth Syst. Sci* 8 (2008) 805–812.  
920 doi:10.5194/nhess-8-805-2008.
- 921 [9] C. Hibert, A. Mangeney, G. Grandjean, N. M. Shapiro, Slope in-  
922 stabilities in Dolomieu crater, Réunion Island: From seismic sig-  
923 nals to rockfall characteristics, *J. Geophys. Res.* 116 (2011) F04032.  
924 doi:10.1029/2011JF002038.
- 925 [10] C. Hibert, A. Mangeney, G. Grandjean, C. Baillard, D. Rivet, N. M.  
926 Shapiro, C. Satriano, A. Maggi, P. Boissier, V. Ferrazzini, W. Crawford,  
927 Automated identification, location, and volume estimation of rockfalls  
928 at piton de la fournaise volcano, *J. Geophys. Res.* 119 (2014) 1082–1105.  
929 doi:10.1002/2013JF002970.
- 930 [11] L. Moretti, A. Mangeney, Y. Capdeville, E. Stutzmann, C. Huggel,  
931 D. Schneider, F. Bouchut, Numerical modeling of the Mount Steller  
932 landslide flow history and of the generated long period seismic waves,  
933 *Geophys. Res. Lett.* 39 (2012). doi:10.1029/2012GL052511.
- 934 [12] V. C. Tsai, B. Minchew, M. P. Lamb, J.-P. Ampuero, A physical model  
935 for seismic noise generation from sediment transport in rivers, *Geophys.*  
936 *Res. Lett.* 39 (2012). doi:10.1029/2011GL050255.
- 937 [13] O. Lengliné, J. E. Elkhoury, G. Daniel, J. Schmittbuhl, R. Tou-  
938 ssaint, J. P. Ampuero, M. Bouchon, Interplay of seismic and  
939 aseismic deformations during earthquake swarms: An experimen-

- 940 tal approach, *Earth Planet. Sc. Lett.* 331-332 (2012) 215–223.  
941 doi:10.1016/j.epsl.2012.03.022.
- 942 [14] M. Stojanova, S. Santucci, L. Vanel, O. Ramos, High frequency moni-  
943 toring reveals aftershocks in subcritical crack growth, *Phys. Rev. Lett.*  
944 112 (2014) 115502. doi:10.1103/PhysRevLett.112.115502.
- 945 [15] G. Michlmayr, D. Cohen, D. Or, Sources and characteristics  
946 of acoustic emissions from mechanically stressed geologic granu-  
947 lar media – A review, *Earth Sc. Rev.* 112 (2012) 97–114.  
948 doi:10.1016/j.earscirev.2012.02.009.
- 949 [16] P. A. Houle, J. P. Sethna, Acoustic Emission from crumpling paper,  
950 *Phys. Rev. E* 54 (1995). doi:S1063-651X9604307-3.
- 951 [17] J. P. Sethna, K. A. Dahmen, C. R. Myers, Crackling Noise, *Nature* 410  
952 (2001) 242–250. doi:10.1038/35065675.
- 953 [18] D. J. Buttle, C. B. Scruby, Characterization of particle im-  
954 pact by quantitative acoustic emission, *Wear* 137 (1990) 63–90.  
955 doi:10.1016/0043-1648(90)90018-6.
- 956 [19] D. J. Buttle, S. R. Martin, C. B. Scruby, Particle sizing by quan-  
957 titative acoustic emission, *Res. Nondestruct. Eval.* 3 (1991) 1–26.  
958 doi:10.1007/BF01606508.
- 959 [20] S. Crampin, Higher modes of seismic surface waves: Second  
960 Rayleigh mode energy, *J. Geophys. Res.* 70 (1965) 5135–5143.  
961 doi:10.1029/JZ070i020p05135.

- 962 [21] G. F. Miller, H. Pursey, On the partition of energy between elastic waves  
963 in a semi-infinite solid, *Proc. R. Soc. Lond. A. Mat.* 233 (1955) 55–69.  
964 doi:10.1098/rspa.1955.0245.
- 965 [22] H. Goyder, R. G. White, Vibrational power flow from machines into  
966 built-up structures, part I: introduction and approximate analyses of  
967 beam and plate-like foundations, *J. Sound Vib.* 68 (1980) 59–75.  
968 doi:10.1016/0022-460X(80)90452-6.
- 969 [23] R. L. Weaver, On diffuse waves in solid media, *J. Acoust. Soc. Am.* 71  
970 (1982). doi:10.1121/1.387816.
- 971 [24] R. L. Weaver, Diffuse waves in finite plates, *J. Sound Vib.* 94 (1984)  
972 319–335. doi:10.5194/nhess-8-805-2008.
- 973 [25] R. L. Weaver, Diffuse elastic waves at a free surface, *J. Acoust. Soc.*  
974 *Am.* 78 (1985). doi:10.1121/1.392576.
- 975 [26] K. Mayeda, L. Malagnini, Source radiation invariant property of local  
976 and near-regional shear-wave coda: Application to source scaling for  
977 the mw 5.9 wells, nevada sequence, *Geophys. Res. Lett.* 37 (2010).  
978 doi:10.1029/2009GL042148.
- 979 [27] R. M. Davies, The determination of static and dynamic yield stresses  
980 using a steel ball, *P. Roy. Soc. Lond. A Mat.* 197 (1949) 416–432.  
981 doi:10.1098/rspa.1949.0073.
- 982 [28] E. Falcon, C. Laroche, S. Fauve, C. Coste, Behavior of one inelastic ball  
983 bouncing repeatedly off the ground, *Eur. Phys. J. B* 3 (1998) 45–57.  
984 doi:10.1007/s100510050283.

- 985 [29] H. Hertz, Über die Berührung fester elastischer Körper (On the vibration  
986 of solid elastic bodies), *J. Reine Angew. Math.* 92 (1882) 156–171.  
987 doi:10.1515/crll.1882.92.156.
- 988 [30] K. Johnson, *Contact Mechanics*, Cambridge University Press, 1985.
- 989 [31] G. C. McLaskey, S. D. Glaser, Hertzian impact: Experimental study  
990 of the force pulse and resulting stress waves, *J. Acoust. Soc. Am.* 128  
991 (2010) 1087. doi:10.1121/1.3466847.
- 992 [32] S. C. Hunter, Energy absorbed by elastic waves during impact, *J. Mech.*  
993 *Phys. Solids* 5 (1957) 162–171. doi:10.1016/0022-5096(57)90002-9.
- 994 [33] J. Reed, Energy losses due to elastic wave propagation dur-  
995 ing an elastic impact, *J. Phys. D Appl. Phys.* 18 (1985) 2329.  
996 doi:10.1088/0022-3727/18/12/004.
- 997 [34] I. M. Hutchings, Energy absorbed by elastic waves during  
998 plastic impact, *J. Phys. D: Appl. Phys.* 12 (1979) 1819.  
999 doi:10.1016/0022-5096(57)90002-9.
- 1000 [35] D. Royer, E. Dieulesaint, *Elastic Waves in Solids I: Free and Guided*  
1001 *Propagation*, Springer, 2000.
- 1002 [36] O. M. Bouthier, R. J. Bernhard, Simple models of the energetics  
1003 of transversely vibrating plates, *J. Sound Vib.* 182 (1995) 149–164.  
1004 doi:10.1006/jsvi.1995.0187.
- 1005 [37] J. Michaels, T. E. Michaels, W. Sachse, Applications of deconvolution  
1006 to acoustic emission signal analysis, *Mater. Eval.* 39 (1981) 1032–1036.

- 1007 [38] G. F. Miller, H. Pursey, The field and radiation impedance of mechanical  
1008 radiators on the free surface of a semi-infinite isotropic solid, Proc. R.  
1009 Soc. Lond. A. Mat. 223 (1954) 521–541. doi:10.1098/rspa.1954.0134.
- 1010 [39] E. Kausel, Lamb’s problem at its simplest, Proc. R. Soc. Lond. A. Mat.  
1011 469 (2013). doi:10.1098/rspa.2012.0462.
- 1012 [40] F. J. Sánchez-Sesma, R. L. Weaver, H. Kawase, S. Matsushima, F. Lu-  
1013 zon, M. Campillo, Energy Partitions among Elastic Waves for Dynamic  
1014 Surface Loads in a Semi-Infinite Solid, Bull. Seism. Soc. Am. 101 (2011)  
1015 1704–1709. doi:10.1785/0120100196.
- 1016 [41] M. Farin, Études expérimentales de la dynamique et de l’émission sis-  
1017 mique des instabilités gravitaires, Ph.D. thesis, IPGP, Paris, 2015.
- 1018 [42] R. Ramírez, T. Pöschel, N. V. Brilliantov, T. Schwager, Coefficient  
1019 of restitution of colliding viscoelastic spheres, Phys. Rev. E 60 (1999)  
1020 4465–4472. doi:10.1103/PhysRevE.60.4465.
- 1021 [43] L. Landau, E. Lifshitz, Theory of Elasticity, volume 7, Pergamon Press,  
1022 1970.
- 1023 [44] A. Fuegel, Statistical calculation and development of glass properties,  
1024 <http://glassproperties.com/>, 2007. (Accessed 10 December 2014).
- 1025 [45] MIT, Material properties database, [http://www.mit.edu/~6.777/  
1026 matprops/pmma.htm](http://www.mit.edu/~6.777/matprops/pmma.htm), 2014. (Accessed 10 December 2014).
- 1027 [46] G. Elert, The physics factbook, [http://hypertextbook.com/facts/  
1028 1999/KatrinaJones.shtml](http://hypertextbook.com/facts/1999/KatrinaJones.shtml), 1999. (Accessed 10 December 2014).

Table 2: Physical values used for calculation of the radiated elastic energy in the glass plate and the concrete block: density  $\rho$ , Young's modulus  $E$ , Poisson ratio  $\nu$ , compressional and shear wave speeds  $c_P$  and  $c_S$ , bending stiffness  $B$ , characteristic distance  $1/\gamma$  and time  $\tau$  of energy attenuation, group velocity  $v_g$  (that depends on the frequency  $f$  (in Hz)), phase velocity  $v_\phi$  and coefficient  $\beta$ . Glass parameters are from Fuegel [44] and PMMA parameters from the MIT material properties database [45]. Elastic parameters  $E$  and  $\nu$  of concrete are estimated from the compressional and shear wave velocities measured through the block and the density  $\rho$  of concrete is from Elert [46].

material		$\rho$ (kg m <sup>-3</sup> )	$E$ (GPa)	$\nu$ -	$c_P$ (m s <sup>-1</sup> )	$c_S$ (m s <sup>-1</sup> )	$B$ (J)	$\gamma$ (1/m)	$\tau$ (s)	$v_g$ (m s <sup>-1</sup> )	$v_\phi$ (m s <sup>-1</sup> )	$\beta$ -
glass	$kh < 1$	2500	74	0.2	5730	3500	4760	$0.014f^{1/6}$	$3.8f^{-2/3}$	$18.6f^{1/2}$	$9.3f^{1/2}$	-
	$kh > 1$							$8.5 \times 10^{-5}f^{2/3}$		3100	3100	
PMMA	$kh < 1$	1180	4.4	0.37	1920	860	357	1	$0.09f^{-1/2}$	$11.7f^{1/2}$	$5.8f^{1/2}$	-
	$kh > 1$							$4.8 \times 10^{-3}f^{2/3}$		$0.15f^{-2/3}$	1400	
concrete	-	2200	16.3	0.4	4030	1620	-	$2.3 \times 10^{-5}f$	$28f^{-1}$	1530	1530	0.3

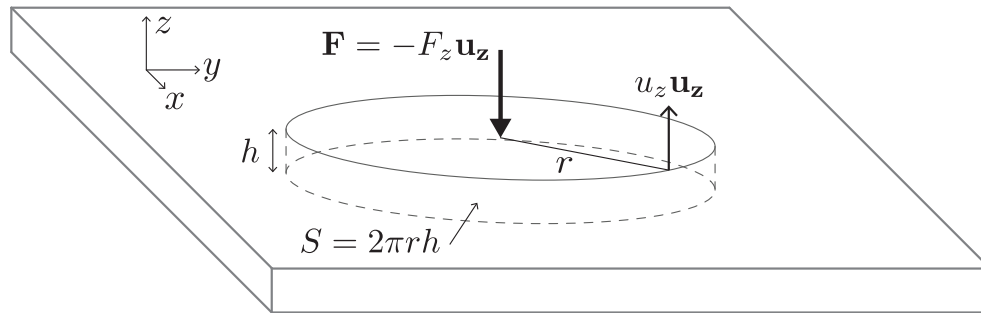


Figure 1: Sketch of the thin plate of thickness  $h$ , characterized by Cartesian coordinates  $x, y, z$ .  $z = 0$  corresponds to the plate free surface. When a normal impact force  $-F_z \mathbf{u}_z$  excites the plate at the origin  $(0, 0, 0)$ , Lamb waves are emitted radially and generate a displacement field  $\mathbf{u} \approx u_z(r, t) \mathbf{u}_z$ .  $S$  is a closed section of the plate, surrounding the impact position and corresponds here to a cylinder of radius  $r$  and height equal to the plate thickness  $h$ .



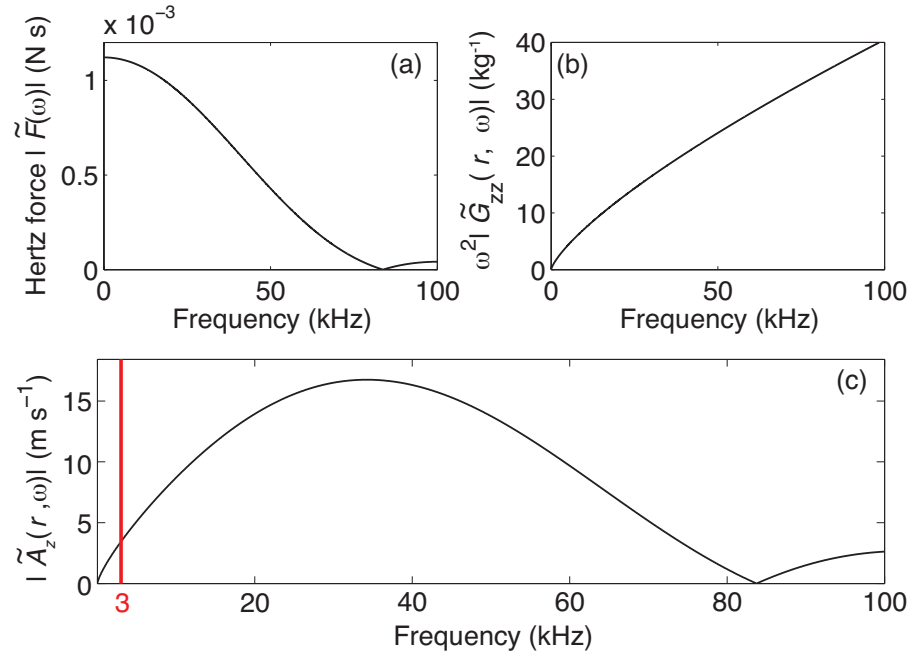


Figure 2: (a) Fourier transform  $|\tilde{F}(\omega)|$  of the ideal Hertz's force of elastic impact of a 4-mm diameter steel sphere on PMMA. (b) Green's function  $|\tilde{G}_{zz}(r, \omega)|$  [equation (12)] at  $r = 10$  cm multiplied by  $\omega^2$  (c) Synthetic amplitude spectrum  $|\tilde{A}_z(r, \omega)|$  obtained by the product of the force in (a) and the function in (b).

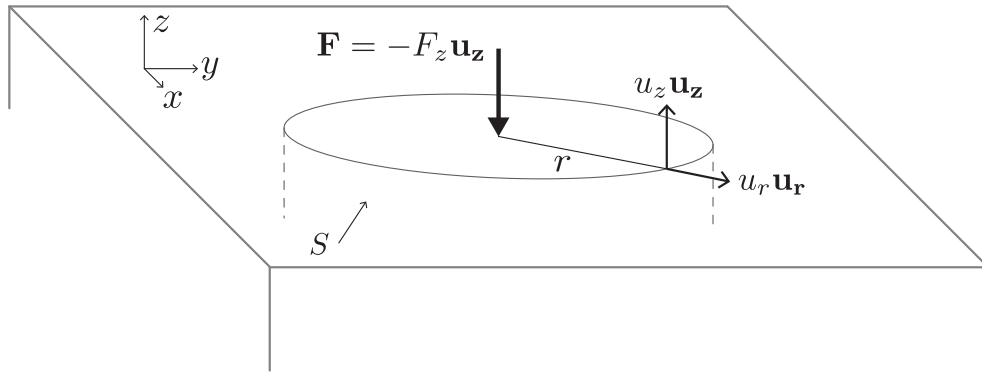


Figure 3: Sketch of the thick block configuration, characterized by Cartesian coordinates  $x, y, z$ .  $z = 0$  corresponds to the block free surface. When a normal impact force  $-F_z \mathbf{u}_z$  excites the block normally at the origin  $(0, 0, 0)$ , Rayleigh waves are emitted radially at the surface and generate a displacement field  $\mathbf{u} = u_r(r, z, t)\mathbf{u}_r + u_z(r, z, t)\mathbf{u}_z$  with an amplitude that decreases exponentially with depth  $z$  (see text).  $S$  is a closed section of the block, surrounding the impact position, and corresponds here to a cylinder of radius  $r$  and infinite height.

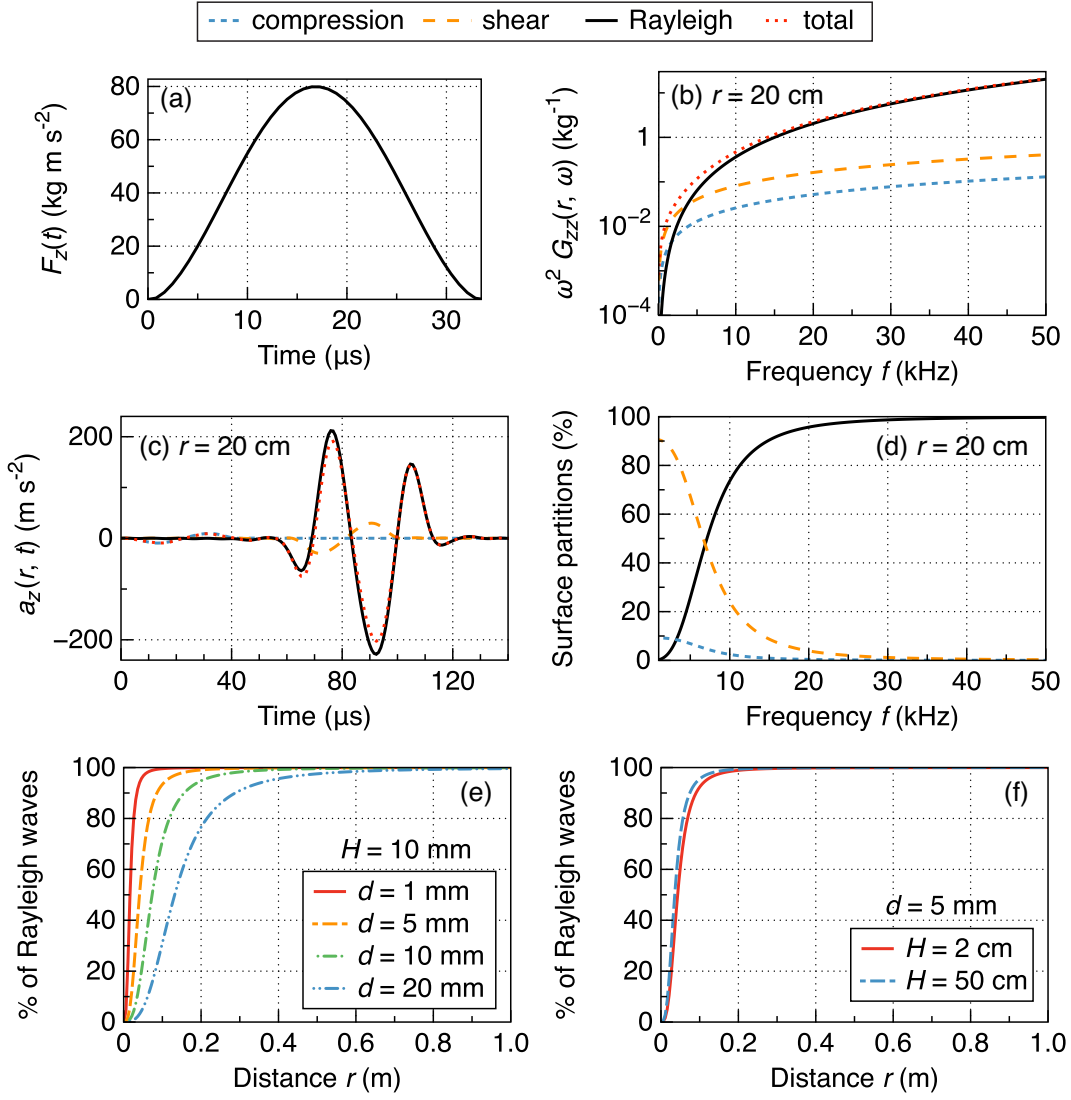


Figure 4: (a) Hertz's force of elastic impact of a steel bead of diameter  $d = 5$  mm dropped from height  $H = 10$  cm on a concrete block is convolved with (b) the Green's functions  $\tilde{G}_{zz}^P$ ,  $\tilde{G}_{zz}^S$  and  $\tilde{G}_{zz}^R$  [equations (19), (20) and (21), respectively], multiplied by  $\omega^2$ , at  $r = 20$  cm from the impact to obtain (c) the synthetic vertical vibration acceleration  $a_z(r, t)$  of each mode at the surface. (d) Percentage of the energy transported by compressional, shear and Rayleigh waves at  $r = 20$  cm from the impact as a function of frequency  $f$ . (e) Percentage  $\pi_{\text{surf}}^R(r)$  of Rayleigh waves in the surface vibration as a function of the distance  $r$  from the impact for (e) a fall height  $H = 10$  cm and different bead diameters  $d$  and (f) for a bead diameter of  $d = 5$  mm and fall heights  $H = 5$  cm and  $H = 50$  cm.

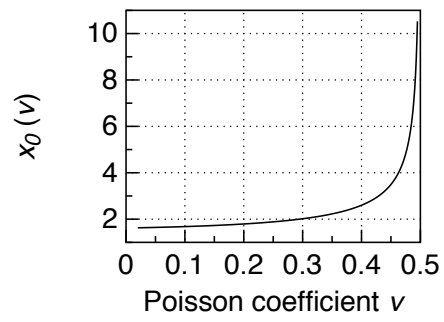


Figure 5: Value of the real solution  $x_0$  of  $f_0(x) = 0$  as a function of Poisson's ratio  $\nu$ .

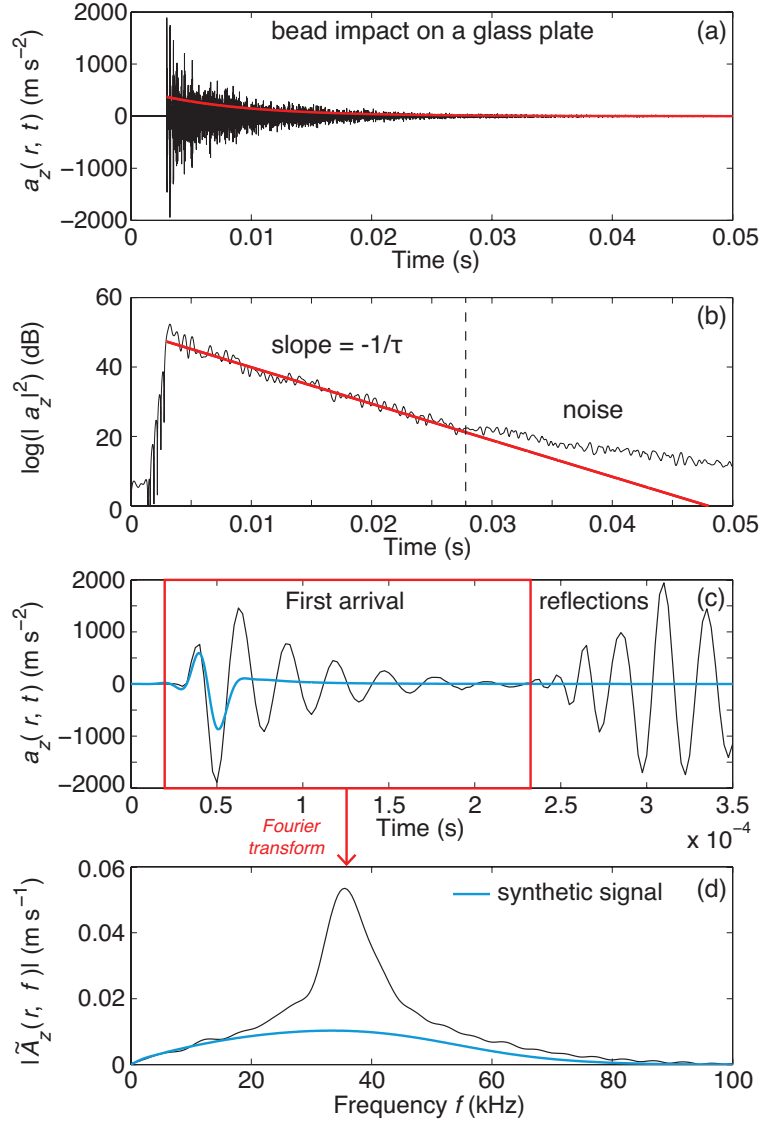


Figure 6: (a)-(c) Normal surface acceleration  $a_z(r, t)$ , filtered below 100 kHz, recorded at  $r = 6$  cm from the source after the impact of a steel bead of diameter 4 mm on the glass plate. (a) and (b) The wave reflects many times off the plate lateral sides and the energy decreases exponentially with time due to viscoelastic dissipation (red line). In (b),  $a_z(r, t)$  is squared, filtered below 2000 Hz and plotted in semi-log form. (c) The plate is sufficiently large to record the first wave arrival entirely (red frame) before the return of the first side reflections. (d) Time Fourier transform  $|\tilde{A}_z(r, f)|$  of the first wave arrival as a function of frequency  $f$ . The thick blue line in (c) and (d) is a synthetic signal obtained with the convolution of the Green's function in equation (12) with the force of Hertz. The discrepancy of the measured signal with theory is discussed in section 4.

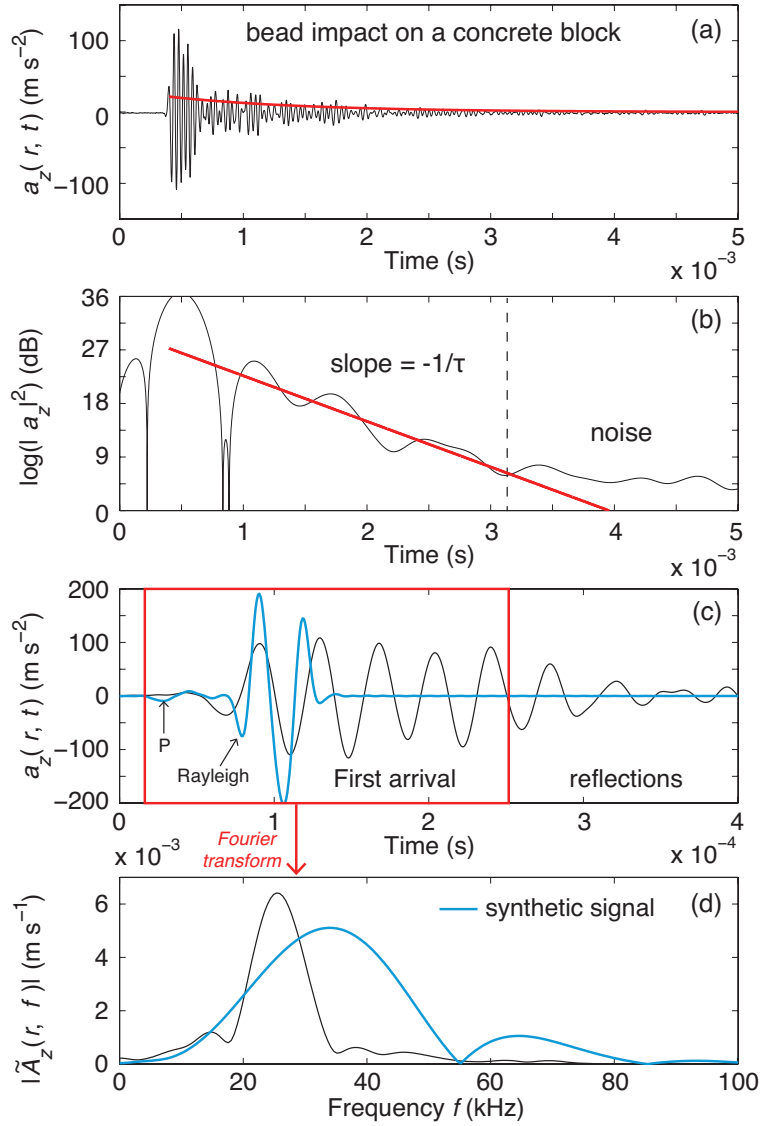


Figure 7: (a)-(c) Normal surface acceleration  $a_z(r, t)$  recorded at  $r = 20$  cm from the source after the impact of a steel bead of diameter 5 mm on the concrete block. (a) and (b) The wave reflects several times off the block boundaries and the energy decreases exponentially with time due to viscoelastic dissipation (red line). In (b),  $a_z(r, t)$  is squared, filtered below 2000 Hz and plotted in semi-log form. (c) The block is sufficiently large to record most of the first wave arrival (red frame) before the return of the first side reflection that should arrive on the right side of the red frame. (d) Time Fourier transform  $|\tilde{A}_z(r, f)|$  of the first wave arrival as a function of frequency  $f$ . The thick blue line in (c) and (d) is a synthetic signal obtained with the convolution of the Green's function in equation (18) with the force of Hertz. In the temporal synthetic signal in (c), we can discern the compressional wave (noted  $P$ ) and the Rayleigh waves. The discrepancy of the measured signal with theory is discussed in section 4.

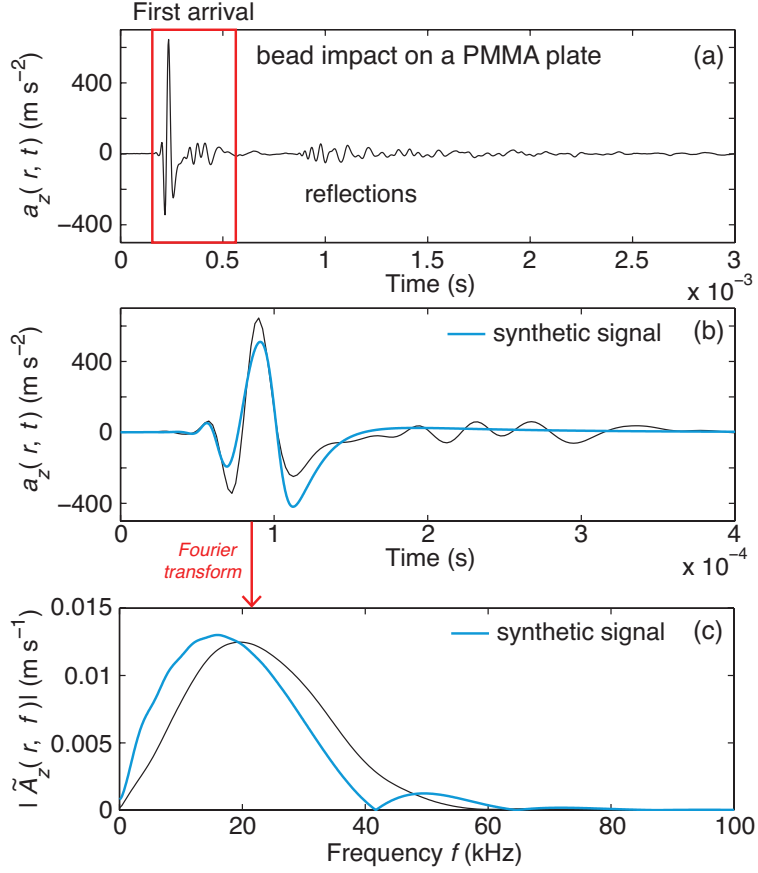


Figure 8: (a) and (b) Normal surface acceleration  $a_z(r, t)$ , filtered below 100 kHz, recorded at  $r = 10$  cm from the source after the impact of a steel bead of diameter 3 mm on the PMMA plate. (a) The direct wave front (red frame) is clearly separated from its reflections off the plate lateral sides. (b) Zoom on the first wave arrival. (c) Time Fourier transform  $|\tilde{A}_z(r, f)|$  of the first wave arrival as a function of the frequency  $f$ . The thick blue line in (b) and (c) is a synthetic signal obtained with the convolution of the Green's function in equation (12) with the force of Hertz. The discrepancy of the measured signal with theory is discussed in section 4.

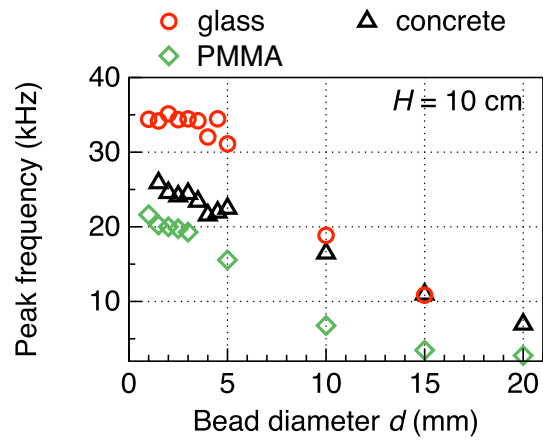


Figure 9: Frequency of the maximum of the amplitude spectrum  $|\tilde{A}_z(r, f)|$ , or peak frequency, for impacts of steel beads of different bead diameters  $d$  on the glass plate, PMMA plate and concrete block. The peak frequency is independent of the fall height in the range investigated.



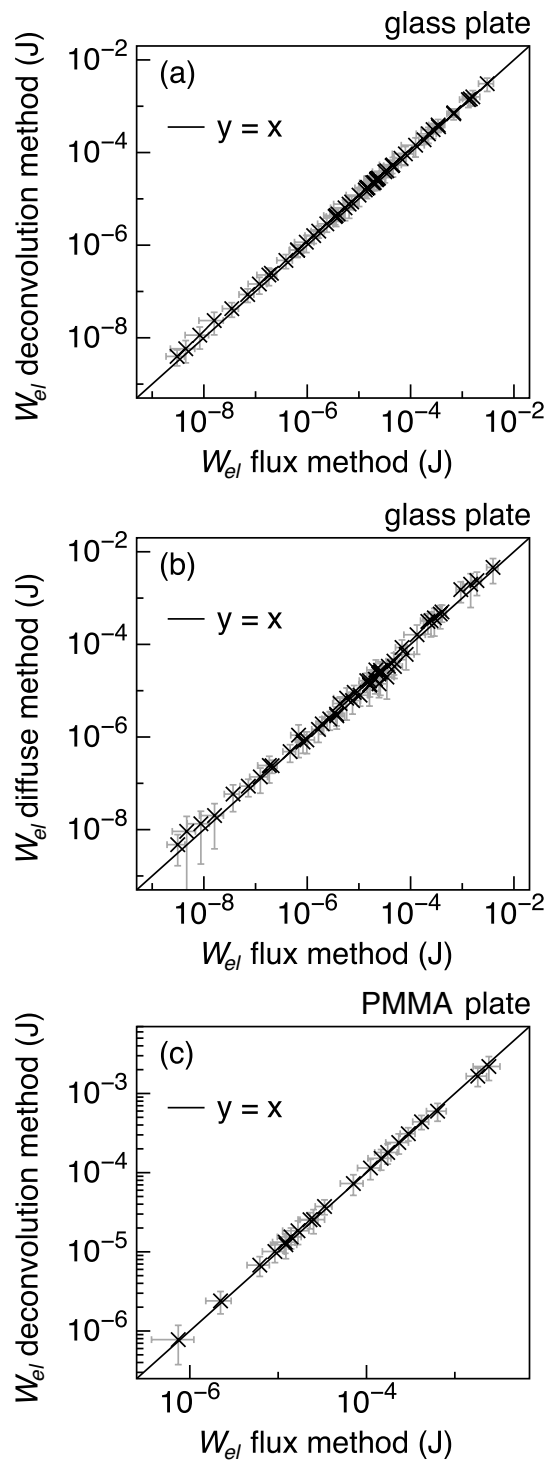


Figure 10: Comparison of the radiated elastic energy  $W_{el}$  calculated using the three methods [equations (8), (13) and (17)] for impacts of steel beads of various diameters from 1 mm to 20 mm dropped from various heights from 2 cm to 25 cm on (a) and (b) the glass plate and (c) the PMMA plate. Error bars ( $\pm 1$  standard deviation) are estimated from reproducibility tests conducted on a series of 12 identical experiments.

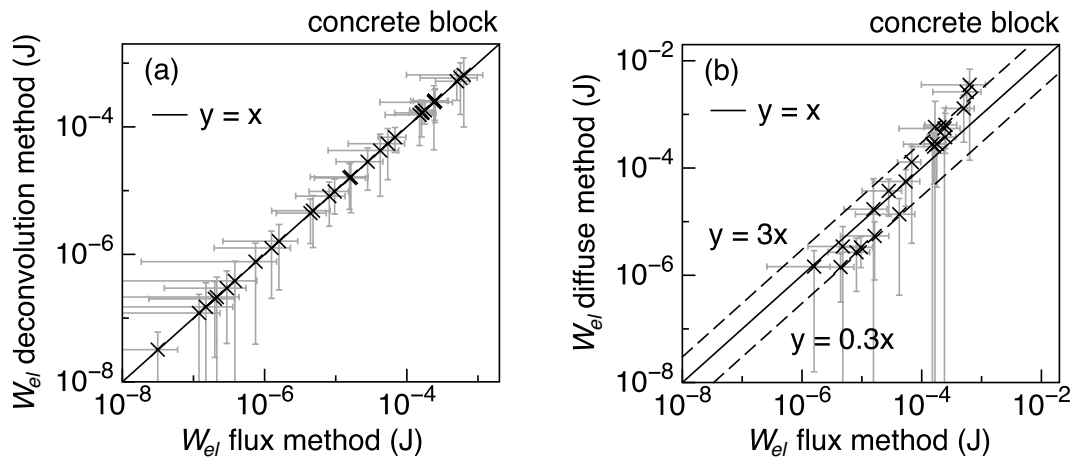


Figure 11: Comparison of the radiated elastic energy  $W_{el}$  calculated using the three methods [equations (31), (35) and (36)] for impacts of steel beads of various diameters from 2 mm to 20 mm dropped from various heights from 5 cm to 43 cm on the concrete block. Error bars ( $\pm 1$  standard deviation) are estimated from reproducibility tests conducted on a series of 12 identical experiments.

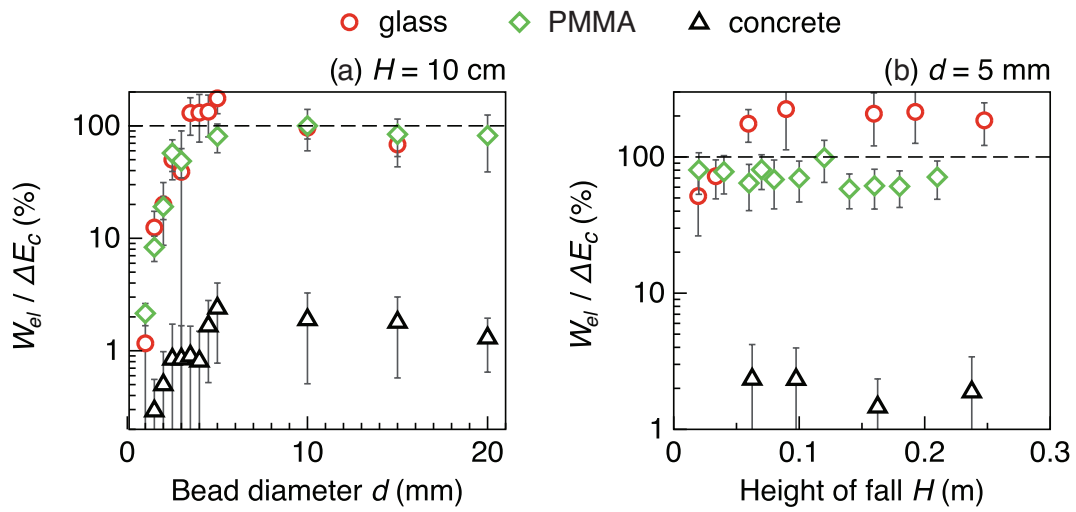


Figure 12: Ratio of the radiated elastic energy  $W_{el}$  to the energy lost during the impact  $\Delta E_c$ , as a function of (a) the bead diameter  $d$  for drops tests from height  $H = 10$  cm and (b) the fall height  $H$  for a bead diameter  $d = 5$  mm, on the glass plate, PMMA plate and concrete block. Error bars ( $\pm 1$  standard deviation) are estimated from reproducibility tests conducted on a series of 12 identical experiments.

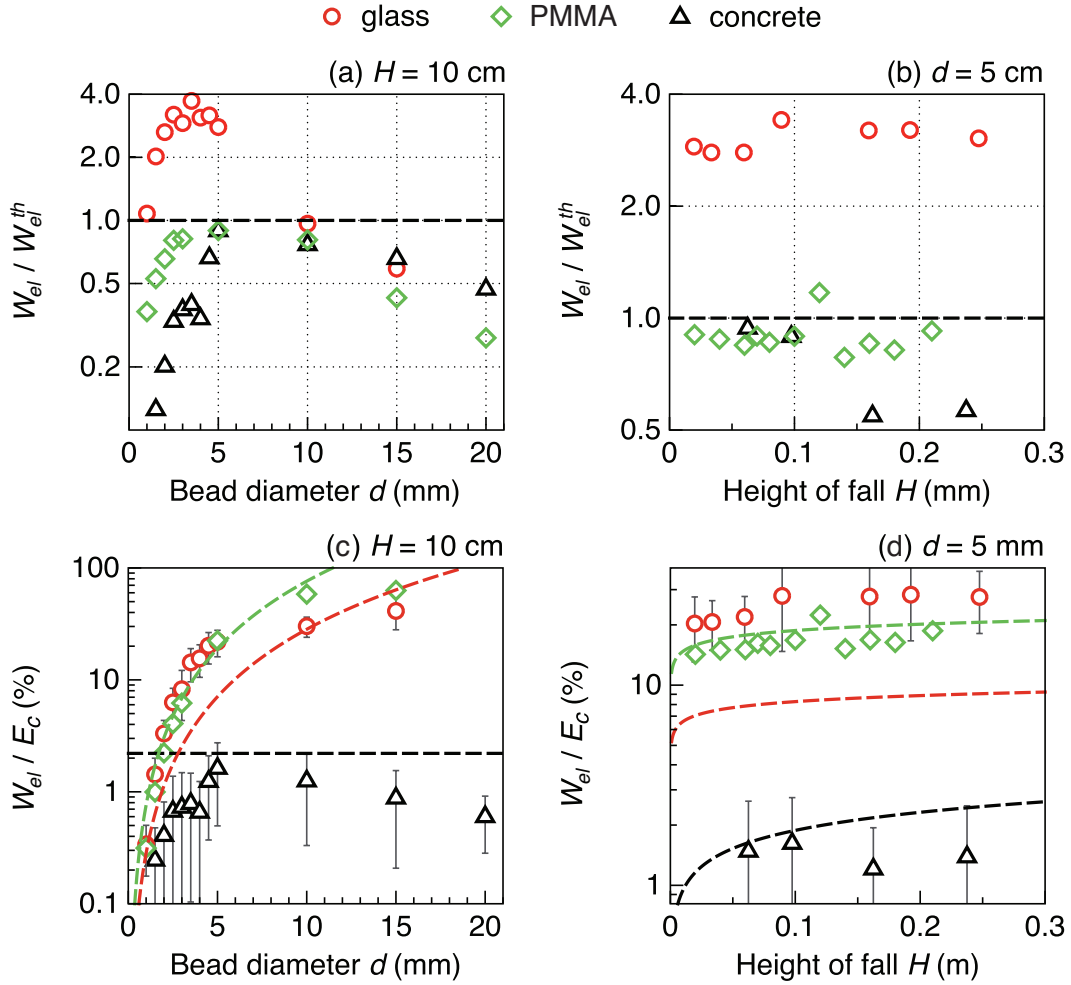


Figure 13: Ratio of the radiated elastic energy  $W_{el}$  measured with the energy flux method (a)-(b) to the theoretical radiated energy  $W_{el}^{th}$  and (c)-(d) to the energy of the impact  $E_c = \frac{1}{2}mV_z^2$ , with  $m$ , the bead mass and  $V_z$ , the impact speed for impacts of steel beads of (a)-(c) different diameters  $d$  for a fall height  $H = 10$  cm and (b)-(d) different fall heights  $H$  for a diameter  $d = 5$  cm, on the glass plate, PMMA plate and concrete block. In Figures (c) and (d), the dashed lines represent the ratio of the theoretical radiated elastic energy  $W_{el}^{th}$  to  $E_c$ .

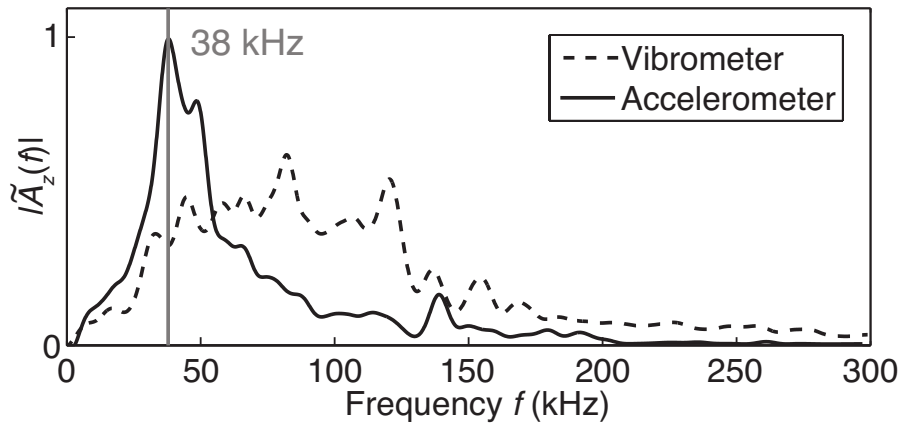


Figure 14: Normalized vibration acceleration  $|\tilde{A}_z(f)|$  generated by the impact of a 3 mm steel bead on the surface of the glass plate. The vibration is recorded by a laser Doppler vibrometer (dashed line) and by the accelerometer used in this study (full line). The system constituted by the glass plate and the accelerometer shows a resonance around 38 kHz. Note that the accelerometer is not very sensitive to the frequencies higher than 100 kHz. However, most of the impacts investigated here generate signals with frequencies lower than 100 kHz. Practically, the laser Doppler vibrometer has a much lower signal to noise ratio than the accelerometer and therefore was not used in this study.

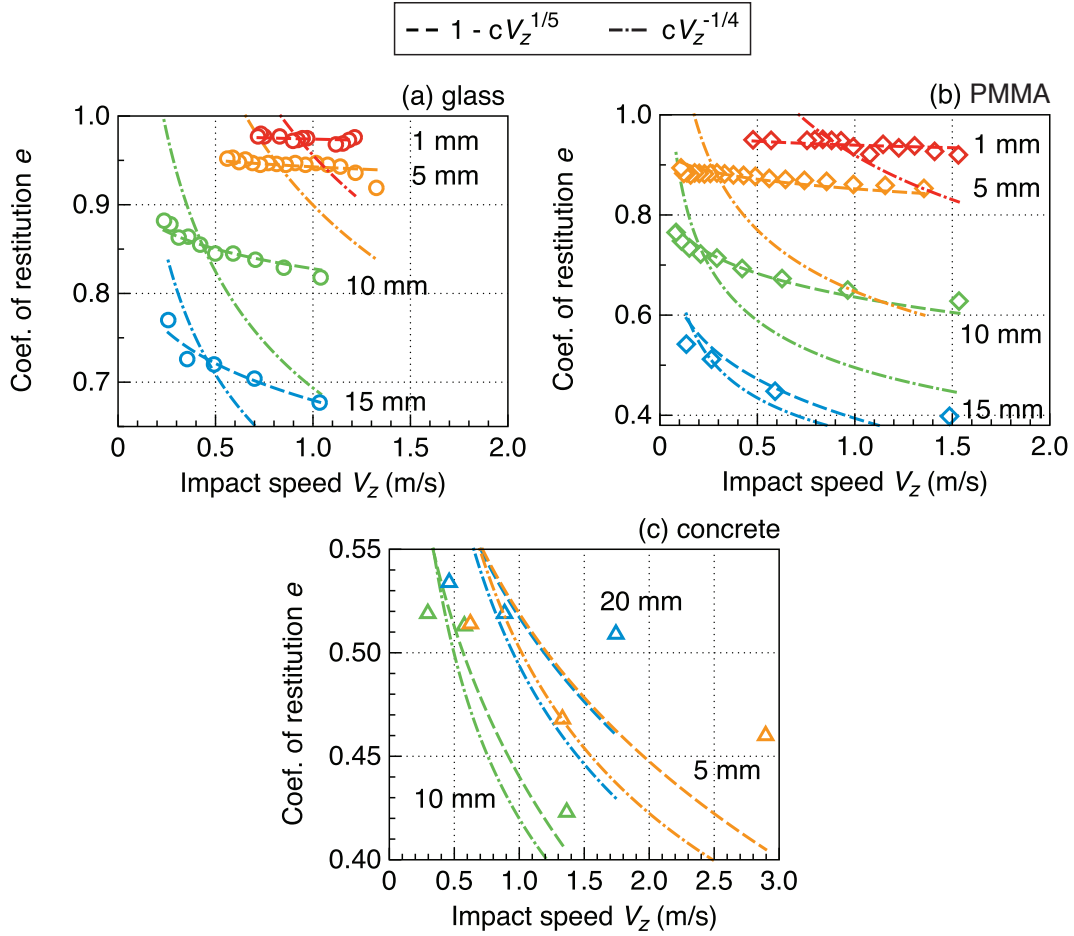


Figure 15: Coefficient of restitution  $e$  as a function of the impact speed  $V_z$  for different bead diameters  $d$  (different colors) on the (a) glass plate, (b) PMMA plate and (c) concrete block. The dashed and dash-dotted lines represent the fitting of the experimental data with the scaling laws  $e = 1 - cV_z^{1/5}$  and  $e = cV_z^{-1/4}$ , respectively, where  $c$  is a constant that depends on the bead diameter.

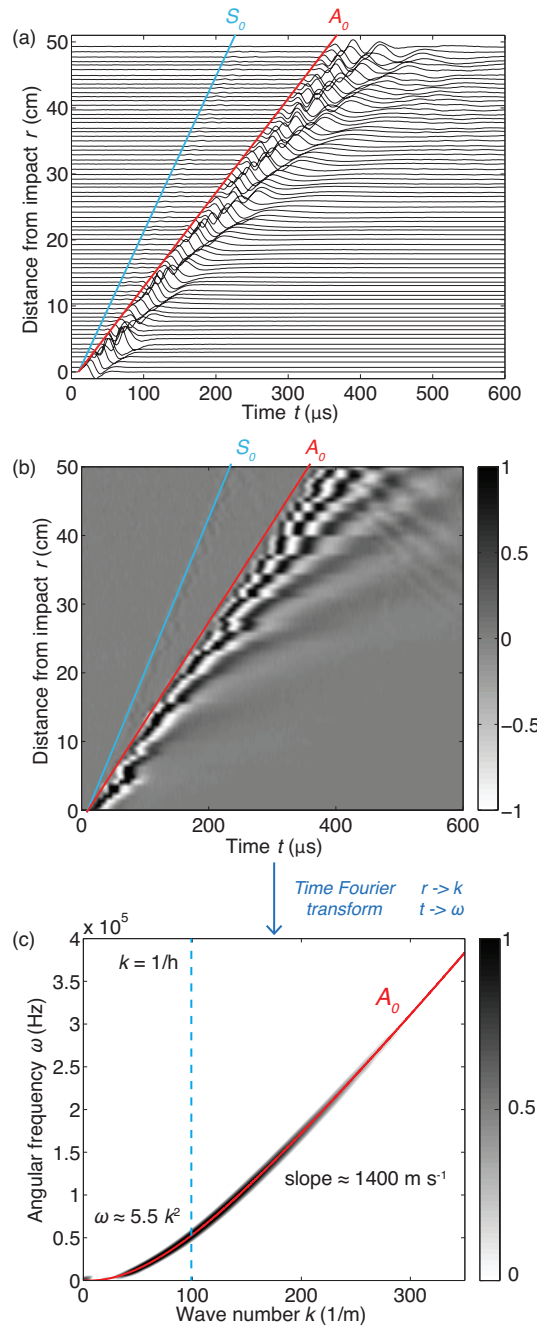


Figure 16: (a) Vibration acceleration  $a_z(r, t)$  recorded at different distances  $r$  from the impact of a 2-mm steel bead on the PMMA plate. The amplitude of each signal is normalized by its maximum value. The red and blue lines indicate the arrival of the Lamb modes  $A_0$  and  $S_0$ , respectively. (b) Matrix representation of the signals of (a). (c) Relation between the angular frequency  $\omega$  and the wave number  $k$  (i.e. dispersion relation), obtained by time and space Fourier transforms of the matrix in (b). Light and dark shading represent respectively low and high power spectral energy (normalized). Red line: theoretical dispersion relation for the fundamental mode of Lamb  $A_0$  in a PMMA plate of thickness  $h = 1$  cm and elastic parameters reported in Table 2.

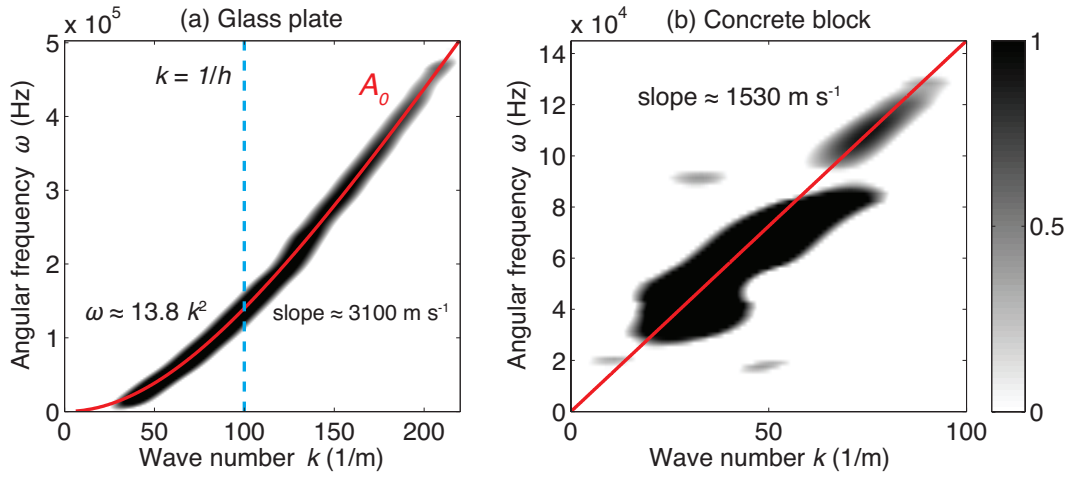


Figure 17: Relation between the angular frequency  $\omega$  and the wave number  $k$  (i.e. dispersion relation) for the direct wave front in (a) the glass plate and (b) the concrete block. Light and dark shading represent respectively low and high power spectral energy (normalized). Red line: (a) theoretical dispersion relation for the fundamental mode of Lamb  $A_0$  in a glass plate of thickness  $h = 1 \text{ cm}$  and elastic parameters reported in Table 2; (b) Linear fit of the data. In the concrete block, the group velocity  $v_g = \partial\omega/\partial k$  equals the phase velocity  $v_\phi = \omega/k$  and is about  $1530 \text{ m s}^{-1}$ .



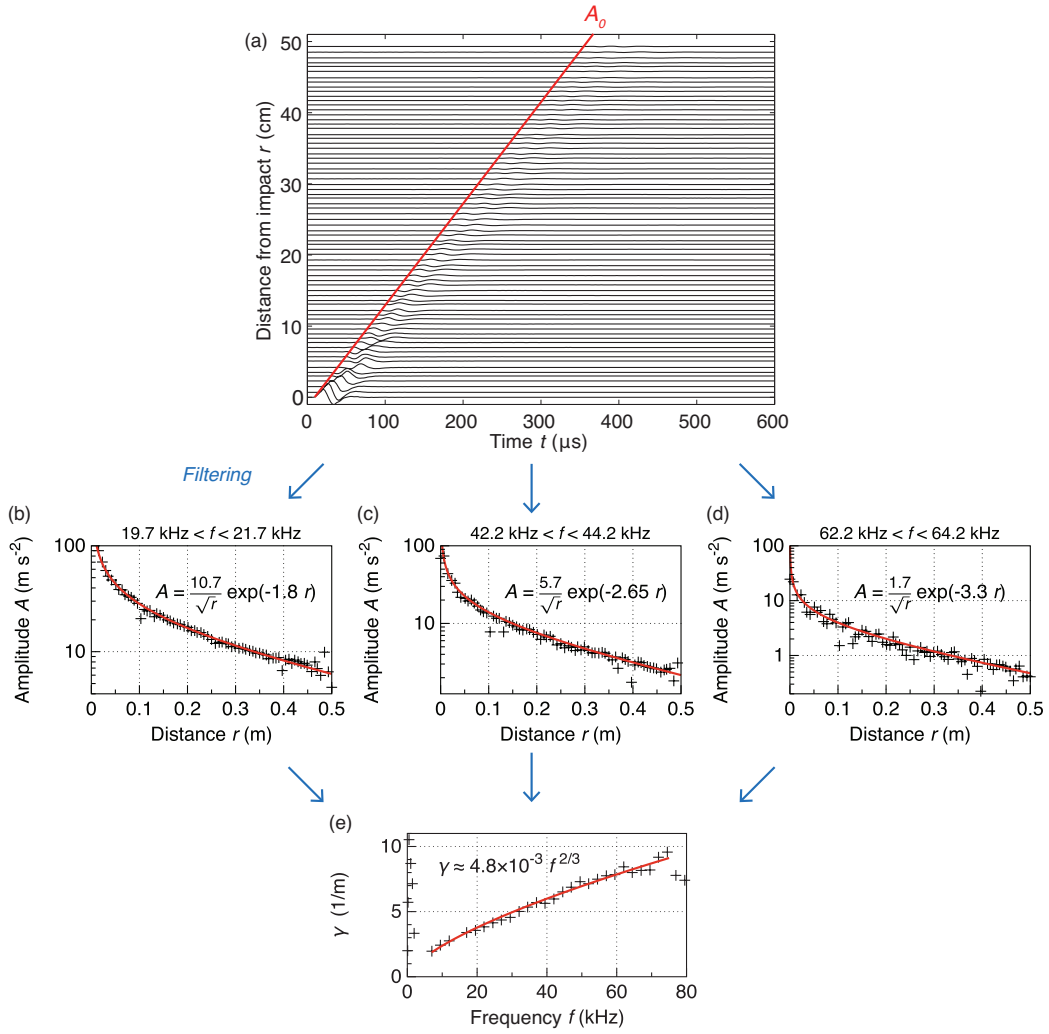


Figure 18: (a) Vibration acceleration  $a_z(r, t)$  recorded at different distances  $r$  from the impact of a 2-mm steel bead on the PMMA plate. (b), (c) and (d) The signals are filtered in different frequency ranges and their maximum amplitude is represented as a function of the distance  $r$ . (e) Attenuation coefficient  $\gamma$  in the PMMA plate as a function of frequency  $f$ .

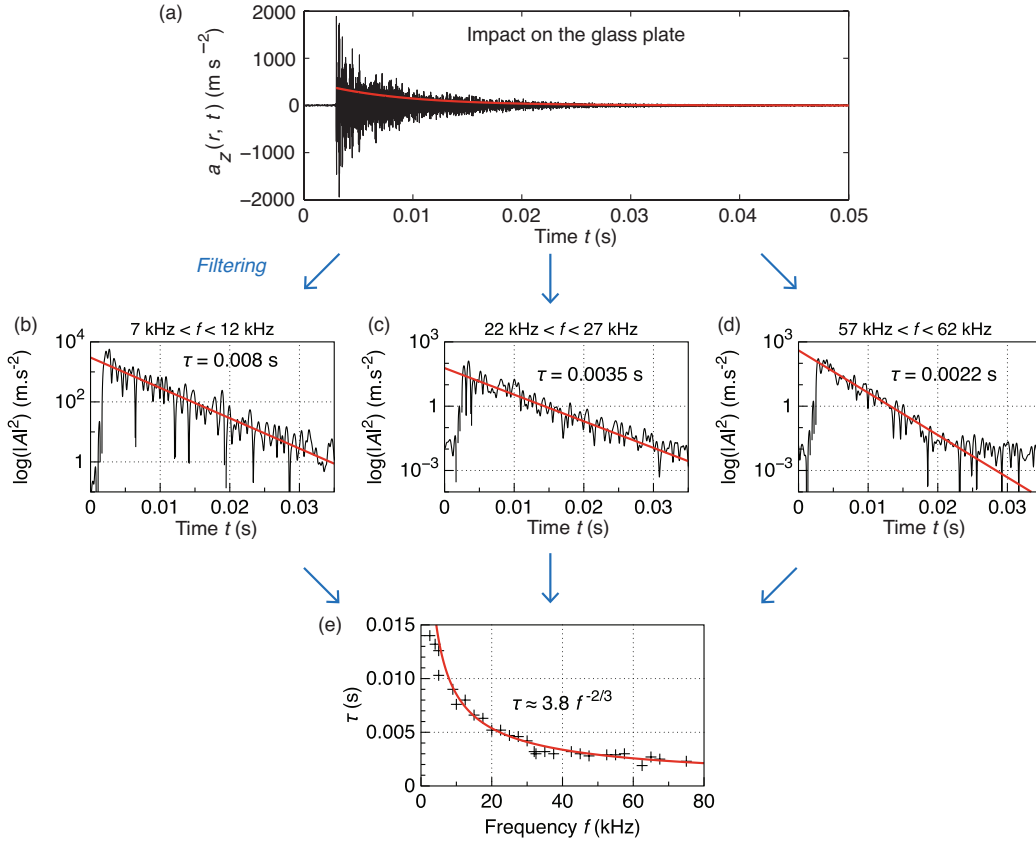


Figure 19: (a) Vibration acceleration  $a_z(r, t)$  generated by the impact of a 4-mm steel bead on the glass plate. (b), (c) and (d) The vibration in (a) is filtered in different frequency ranges. The envelope of the squared vibration averaged over several periods decreases exponentially with time and the inverse of the slope in semi-logarithmic scale (red line) is the characteristic time  $\tau$ . (e)  $\tau$  as a function of frequency  $f$  in the glass plate.

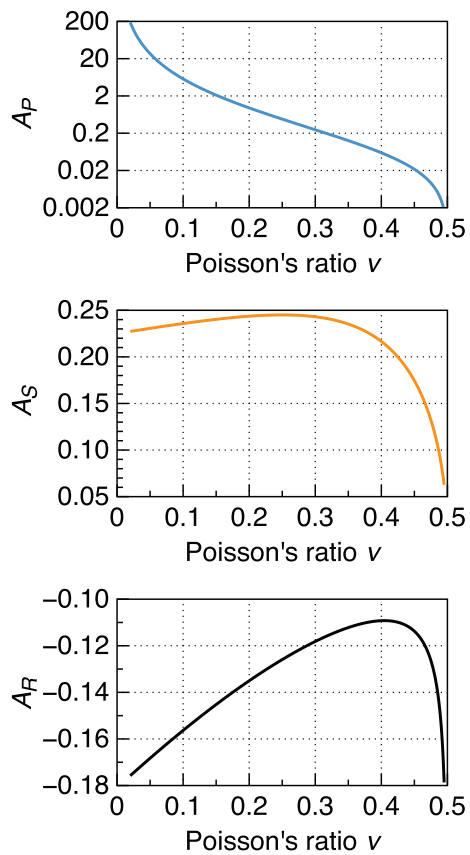


Figure 20: Values of the coefficient  $A_P$ ,  $A_S$  and  $A_R$  as a function of Poisson's ratio  $\nu$ .

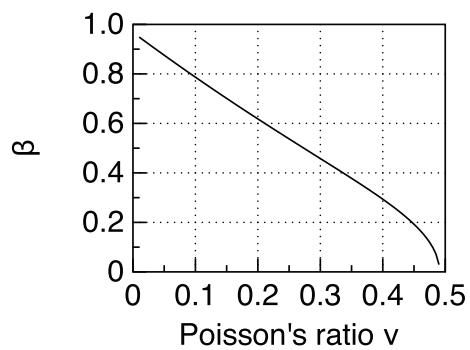


Figure 21: Coefficient  $\beta$  defined by equation (33) as a function of the Poisson ratio  $\nu$ .